Computers in Biology and Medicine 142 (2022) 105203

Contents lists available at ScienceDirect

Computers in Biology and Medicine

journal homepage: www.elsevier.com/locate/compbiomed

The role of mechano-electric feedbacks and hemodynamic coupling in scar-related ventricular tachycardia

Matteo Salvador [a,*], Francesco Regazzoni [a], Stefano Pagani [a], Luca Dede' [a], Natalia Trayanova [b], Alfio Quarteroni [a,c]

[a] MOX-Dipartimento di Matematica, Politecnico di Milano, Milan, Italy
[b] Department of Biomedical Engineering, Johns Hopkins University, Baltimore, MD, USA
[c] École Polytechnique Fédérale de Lausanne, Lausanne, Switzerland

ARTICLE INFO

Keywords:
Cardiac electromechanics
Numerical simulations
Mechano-electric feedback
Stretch-activated channels
Ventricular tachycardia

ABSTRACT

Mechano-electric feedbacks (MEFs), which model how mechanical stimuli are transduced into electrical signals, have received sparse investigation by considering electromechanical simulations in simplified scenarios. In this paper, we study the effects of different MEFs modeling choices for myocardial deformation and nonselective stretch-activated channels (SACs) in the monodomain equation. We perform numerical simulations during ventricular tachycardia (VT) by employing a biophysically detailed and anatomically accurate 3D electromechanical model for the left ventricle (LV) coupled with a 0D closed-loop model of the cardiocirculatory system. We model the electromechanical substrate responsible for scar-related VT with a distribution of infarct and peri-infarct zones. Our mathematical framework takes into account the hemodynamic effects of VT due to myocardial impairment and allows for the classification of their hemodynamic nature, which can be either stable or unstable. By combining electrophysiological, mechanical and hemodynamic models, we observe that all MEFs may alter the propagation of the transmembrane potential. In particular, we notice that the presence of myocardial deformation in the monodomain equation may change the VT basis cycle length and the conduction velocity but do not affect the hemodynamic nature of the VT. Finally, nonselective SACs may affect VT stability, by possibly turning a hemodynamically stable VT into a hemodynamically unstable one.

1. Introduction

Cardiac arrhythmias result from an irregular electrical activity of the human heart. Among them, ventricular tachycardia (VT), which manifests with an accelerated heart rate, is one of the most life-threatening rhythm disorders. VT may be classified as either hemodynamically stable or unstable, depending on the capability of the heart to effectively pump blood in the circulatory system. While stable VT is generally tolerated by patients and can be treated with antiarrhythmic drugs, unstable VT is associated to serious symptoms, such as chest pain, shortness of breath or loss of consciousness, and usually requires immediate medical attention and cardioversion [21]. According to the specific pathogenesis, the stability of the VT remains the same or changes over time. Moreover, it may also degenerate towards ventricular fibrillation (VF), a life-threatening condition in which the ventricular activity is fully disorganized and chaotic, leading to heart failure [63].

These pathological conditions are difficult to explore in patients in the clinical framework. Biophysically detailed computational heart models could be used to provide a deeper understanding of the hemodynamic response to VT and to characterize the electromechanical substrate leading to life-threatening arrhythmias.

While electrophysiological simulations are well-established for scar-related VT identification and treatment on human ventricles [1,10,19,47], patient-specific electromechanical models coupled with closed-loop cardiovascular circulation have been just recently used for the first time to enhance our knowledge on VT [62]. Indeed, on one side, the physiological processes by which the mechanical behavior alters the electrical activity of the human heart, known as mechano-electric feedbacks (MEFs), are relevant and not fully elucidated [13,32,34,65,67,70,71]. On the other hand, the identification of the hemodynamic nature of the VT has significant clinical implications [62].

The goal of this study is threefold: (1) to combine electrophysiology, activation, mechanics and hemodynamics in several numerical

* Corresponding author.
E-mail address: matteo1.salvador@polimi.it (M. Salvador).

https://doi.org/10.1016/j.compbiomed.2021.105203
Received 29 October 2021; Received in revised form 29 December 2021; Accepted 29 December 2021
Available online 4 January 2022

simulations of scar-related VT, with the aim of uncovering the roles of myocardial deformation and the recruitment of SACs on VT stability; (2) to show that our computational model effectively reproduces both hemodynamically stable and hemodynamically unstable VT; (3) to capture relevant microscopic mechanisms during VT, such as the incomplete relaxation of sarcomeres, given the biophysical detail of our electromechanical model.

2. Mathematical models

We provide an overview of the 3D cardiac electromechanical model coupled with a 0D closed-loop model of the cardiovascular system (see Refs. [56,62]).

We depict in Fig. 1 the computational domain Ω_0, which represents a human left ventricle (LV) taken from the Zygote Solid 3D heart model [29]. Its boundary $\partial\Omega_0$ is partitioned into epicardium Γ_0^{epi}, endocardium Γ_0^{endo} and base Γ_0^{base}. We recall that $\partial\Omega_0 = \overset{\text{- epi}}{\Gamma_0} \cup \overset{\text{- endo}}{\Gamma_0} \cup \overset{\text{- base}}{\Gamma_0}$.

2.1. 3D-0D closed-loop electromechanical model

We consider a multiphysics and multiscale 3D-0D mathematical framework comprised of four different core models, that we describe in Sections 2.1.1- 2.1.4. These respectively include cardiac electrophysiology ($\mathscr{E}$) [12,14,37,41], mechanical activation ($\mathscr{A}$) [35,40,52,59,60], passive mechanics ($\mathscr{M}$) [24,25,28,42] and blood circulation ($\mathscr{C}$) [3,4,8,27,33,51,56]. A volume constraint ($\mathscr{V}$), that we introduce in Section 2.1.4, defines the coupling condition between the LV cardiac electromechanics and the remaining part of cardiovascular system [56]. All these models represent several physiological processes, ranging from the cellular level to the organ scale.

2.1.1. Electrophysiology ($\mathscr{E}$)

We model the electrical activity of the myocardium by means of the monodomain equation coupled with the ten Tusscher Panfilov (TTP06) ionic model, suitable for the human ventricular action potential [9,12,38,66]:

$$(\mathscr{E}_{\text{gMEF-full, SAC}})\begin{cases} J\chi_{\text{m}}\left[C_{\text{m}}\dfrac{\partial u}{\partial t} + \mathcal{I}_{\text{ion}}(u,\boldsymbol{w}) + \mathcal{I}_{\text{SAC}}(u,\mathbf{F})\right] - \nabla\cdot(J\mathbf{F}^{-1}\boldsymbol{D}\,\mathbf{F}^{-T}\nabla u) = J\chi_{\text{m}}\mathcal{I}_{\text{app}}(t) & \text{in } \Omega_0\times(0,T], \\ \dfrac{\partial \boldsymbol{w}}{\partial t} - \boldsymbol{H}(u,\boldsymbol{w}) = \mathbf{0} & \text{in } \Omega_0\times(0,T], \\ \left(J\mathbf{F}^{-1}\boldsymbol{D}\,\mathbf{F}^{-T}\nabla u\right)\cdot\mathbf{N} = 0 & \text{on } \partial\Omega_0\times(0,T], \end{cases} \tag{1}$$

where u is the transmembrane potential and $\boldsymbol{w}$ is the vector containing both gating and ionic variables. χ_{m} is the surface area-to-volume ratio of cardiomyocytes, C_{m} represents the transmembrane capacitance per unit area. The applied current $\mathcal{I}_{\text{app}}$ mimics the effect of the Purkinje network [18,36,72] and allows for the application of a pacing protocol, by triggering the action potential at specific locations of the myocardium. The reaction terms $\mathcal{I}_{\text{ion}}$ and $\boldsymbol{H}$ couple the propagation of the transmembrane potential to the cellular dynamics. Indeed, they allow to accurately describe ions dynamics across the cell membrane. The expressions for both the ionic current $\mathcal{I}_{\text{ion}}$ and the vector-valued function $\boldsymbol{H}$, the latter accounting for a system of 18 ordinary differential equations (ODEs), can be found in the original paper of the TTP06 ionic model [66]. Furthermore, Eq. (1) is equipped with homogeneous Neumann boundary conditions for u at the boundary $\partial\Omega_0$, which defines the condition of electrically isolated domain for Ω_0. $\boldsymbol{D}$ represents the conductivity tensor, that reads:

$$\boldsymbol{D} = \eta\sigma_{\text{l}}\frac{\mathbf{f}_0\otimes\mathbf{f}_0}{\|\mathbf{f}_0\|^2} + \eta\sigma_{\text{t}}\frac{\mathbf{s}_0\otimes\mathbf{s}_0}{\|\mathbf{s}_0\|^2} + \eta\sigma_{\text{n}}\frac{\mathbf{n}_0\otimes\mathbf{n}_0}{\|\mathbf{n}_0\|^2}, \tag{2}$$

where σ_{l}, σ_{t}, σ_{n} are the longitudinal, transversal and normal conductivities, respectively. The parameter $\eta = \eta(\boldsymbol{x}) \in [0, 1]$ takes into account the effect of scars, grey zones and non-remodeled regions. This parameter is also incorporated inside the formulation of the TTP06 model, as described in Ref. [62]. Specifically, we model scars as myocardial regions where no evolution of both the transmembrane potential and all ionic variables occur (Eq. (1) is not solved, $\eta = 0$). Then, we consider a continuum of grey zones using linear interpolation, for $\eta \in [0.1, 1]$, going from the full healthy case ($\eta = 1$) to the grey zone described in Ref. [1] ($\eta = 0.1$), where G_{Na}, G_{CaL}, G_{kr} and G_{ks} conductances are reduced to 38%, 31%, 30% and 20% of their physiological values, respectively.

The deformation tensor $\mathbf{F} = \mathbf{I} + \nabla\mathbf{d}$ and its determinant $J = \det(\mathbf{F})$ are needed to perform the mechano-electric coupling [69]. Indeed, we model the so called mechano-electric feedbacks (MEFs) [17,26]. The geometry-mediated MEFs incorporate the effects of displacement $\mathbf{d}$ on the cardiac tissue, while other physiological processes act at the level of single cardiomyocytes [37,70]. Among them, some examples are selective (e.g. K^+-permeable) or nonselective SACs and intracellular calcium $[Ca^{2+}]_{\text{i}}$ binding to sarcolemmal buffers, the latter requiring more sophisticated ventricular ionic models [5,68]. In this paper we model nonselective SACs by means of the following formulation [37]:

$$\mathcal{I}_{\text{SAC}}(u,\mathbf{F}) = G_{\text{s}}(\|\mathbf{f}_0\| - 1)_+(u - u_{\text{rev}}), \tag{3}$$

where G_{s} and u_{rev} represent the conductance of the channels and the reversal potential, respectively. SACs may alter the shape of the action potential (AP) by lengthening or shortening its duration (APD) and by generating higher resting potentials. This may induce early or delayed afterdepolarizations (EADs or DADs) and premature excitation.

Both geometry-mediated MEFs and nonselective SACs are generally

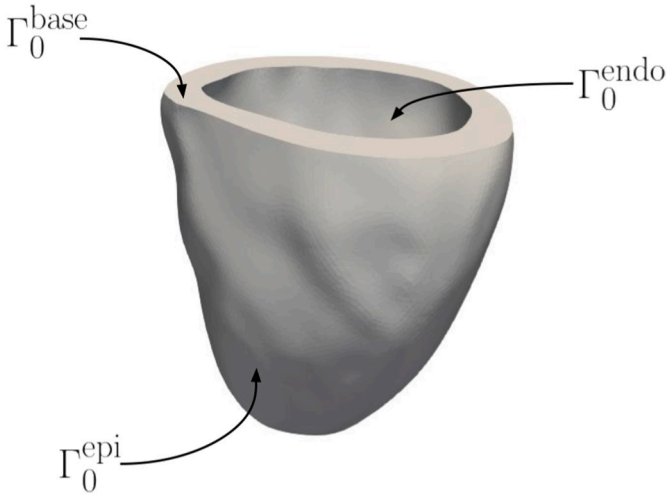

Fig. 1. Computational domain Ω_0, given by a human LV.

Table 1
Modeling choices for the monodomain equation that have been used in this paper. We consider different parametrizations for $\mathcal{I}_{\text{SAC}}(u,\mathbf{F})$ in terms of G_s and u_{rev}. $\boldsymbol{D}_{\mathbf{I}}$ indicates the conductivity tensor in Eq. (2) with $\mathbf{F}=\mathbf{I}$. Indeed, MEFs inside the formulation of the conductivity tensor are neglected for $(\mathscr{E}_{\text{gMEF-minimal}})$ and $(\mathscr{E}_{\text{SAC}})$.

Model name	Equation
$(\mathscr{E})$	$\chi_m\left[C_m\frac{\partial u}{\partial t}+\mathcal{I}_{\text{ion}}(u,\boldsymbol{w})\right]-\nabla\cdot(\boldsymbol{D}_{\mathbf{I}}\nabla u)=\chi_m\mathcal{I}_{\text{app}}(t)$
$(\mathscr{E}_{\text{gMEF-minimal}})$	$\chi_m\left[C_m\frac{\partial u}{\partial t}+\mathcal{I}_{\text{ion}}(u,\boldsymbol{w})\right]-\nabla\cdot(J\mathbf{F}^{-1}\boldsymbol{D}_{\mathbf{I}}\mathbf{F}^{-T}\nabla u)=\chi_m\mathcal{I}_{\text{app}}(t)$
$(\mathscr{E}_{\text{gMEF-enhanced}})$	$\chi_m\left[C_m\frac{\partial u}{\partial t}+\mathcal{I}_{\text{ion}}(u,\boldsymbol{w})\right]-\nabla\cdot(J\mathbf{F}^{-1}\boldsymbol{D}\mathbf{F}^{-T}\nabla u)=\chi_m\mathcal{I}_{\text{app}}(t)$
$(\mathscr{E}_{\text{gMEF-full}})$	$J\chi_m\left[C_m\frac{\partial u}{\partial t}+\mathcal{I}_{\text{ion}}(u,\boldsymbol{w})\right]-\nabla\cdot(J\mathbf{F}^{-1}\boldsymbol{D}\mathbf{F}^{-T}\nabla u)=J\chi_m\mathcal{I}_{\text{app}}(t)$
$(\mathscr{E}_{\text{SAC}})$	$\chi_m\left[C_m\frac{\partial u}{\partial t}+\mathcal{I}_{\text{ion}}(u,\boldsymbol{w})+\mathcal{I}_{\text{SAC}}(u,\mathbf{F})\right]-\nabla\cdot(\boldsymbol{D}_{\mathbf{I}}\nabla u)=\chi_m\mathcal{I}_{\text{app}}(t)$
$(\mathscr{E}_{\text{gMEF-full, SAC}})$	$J\chi_m\left[C_m\frac{\partial u}{\partial t}+\mathcal{I}_{\text{ion}}(u,\boldsymbol{w})+\mathcal{I}_{\text{SAC}}(u,\mathbf{F})\right]-\nabla\cdot(J\mathbf{F}^{-1}\boldsymbol{D}\mathbf{F}^{-T}\nabla u)=J\chi_m\mathcal{I}_{\text{app}}(t)$

known to be pro-arrhythmic in pathological scenarios, because they increase the likelihood of having extra stimuli during cardiac contraction and relaxation [70].

In this work we consider Eq. (1) with several degrees of complexity to assess similarities and differences in the outcomes of the electromechanical simulations during VT. We report in Table 1 the mathematical models and the parametrizations that we consider. In particular, the choice of three different mathematical models for the geometry-mediated MEFs, namely $(\mathscr{E}_{\text{gMEF-minimal}})$, $(\mathscr{E}_{\text{gMEF-enhanced}})$ and $(\mathscr{E}_{\text{gMEF-full}})$, is motivated by the numerous formulations of this type of feedback that can be found in the literature [11,15,37,50]. Indeed, we range from minimal to complete inclusion of geometry-mediated MEFs in the monodomain equation.

2.1.2. Activation $(\mathscr{A})$

To model how the calcium wave following the AP triggers a series of chemo-mechanical reactions within sarcomeres, resulting in the generation of an active force in the muscle, we use the mean-field version of the model proposed in Ref. [52], henceforth denoted by RDQ20-MF. Its mathematical formulation can be written in the following compact form:

$$(\mathscr{A})\quad \frac{\partial \mathbf{s}}{\partial t}=\boldsymbol{K}\left(\mathbf{s},[Ca^{2+}]_i,SL,\frac{\partial SL}{\partial t}\right)\text{in }\Omega_0\times(0,T], \tag{4}$$

where $\mathbf{s}$ represents a vector of states variables. This mathematical model is based on a biophysically accurate description of regulatory and contractile proteins and their dynamics. Thanks to suitable dimensionality reduction techniques, the dynamics of stochastic processes underlying both chemical and mechanical microscale transitions are described in only 20 ODEs (that is $\mathbf{s}(t)\in\mathbb{R}^{20}$). The computational cost of this model is thus comparable to that of phenomenological models [35,39,58], while providing a biophysically detailed description that is consistent with the level of detail and mechanistic understanding of the ionic model needed for the present study.

The inputs of the RDQ20-MF model are the intracellular calcium concentration $[Ca^{2+}]_i$ coming from $(\mathscr{E})$, the sarcomere length (denoted by SL) and its time derivative (the latter allows to account for the so-called force-velocity relationship [31]). The variable SL is obtained as $SL=SL_0\sqrt{\mathcal{I}_{4f}}$, where SL_0 is the sarcomere slack length and the fourth invariant $\mathcal{I}_{4f}=\mathbf{f}_0\cdot\mathbf{f}_0$ measures the tissue stretch in the fiber direction. Finally, the output of the RDQ20-MF model is the active tension generated at the microscale, that can be obtained as $T_a(\mathbf{s},SL)$.

Differently from Ref. [62], here we consider a biophysically detailed active stress model. For this reason, we do not need to put the parameter η inside its parametrization. Indeed, the active force generation mechanisms are properly handled by the active stress model, which receives different intracellular calcium waves from $(\mathscr{E})$ according to the specific area of the myocardium (scar, grey zone or healthy) and provides physiological values of active tension in all cases.

2.1.3. Mechanics $(\mathscr{M})$

We employ the momentum conservation equation to model the dynamics of the displacement $\mathbf{d}$ of the myocardium:

$$(\mathscr{M})\begin{cases}\rho_s\dfrac{\partial^2\mathbf{d}}{\partial t^2}-\nabla\cdot\mathbf{P}(\mathbf{d},T_a(\mathbf{s},SL))=\mathbf{0} & \text{in }\Omega_0\times(0,T],\\ \mathbf{P}(\mathbf{d},T_a(\mathbf{s},SL))\mathbf{N}=\mathbf{K}^{\text{epi}}\mathbf{d}+\mathbf{C}^{\text{epi}}\dfrac{\partial\mathbf{d}}{\partial t} & \text{on }\Gamma_0^{\text{epi}}\times(0,T],\\ \mathbf{P}(\mathbf{d},T_a(\mathbf{s},SL))\mathbf{N}=-p_{\text{LV}}(t)\,J\mathbf{F}^{-T}\mathbf{N} & \text{on }\Gamma_0^{\text{endo}}\times(0,T],\\ \mathbf{P}(\mathbf{d},T_a(\mathbf{s},SL))\mathbf{N}=|J\mathbf{F}^{-T}\mathbf{N}|\mathbf{v}_{\text{LV}}^{\text{base}}(t) & \text{on }\Gamma_0^{\text{base}}\times(0,T].\end{cases} \tag{5}$$

We also consider the hyperelasticity assumption, so that the strain energy function can be differentiated with respect to the deformation tensor $\mathbf{F}$ to obtain $\mathbf{P}$ [24,42]. In the mechanical model $(\mathscr{M})$, ρ_s represents the density of the myocardium. The Piola-Kirchhoff stress tensor $\mathbf{P}=\mathbf{P}(\mathbf{d},T_a)$ is additively decomposed according to:

$$\mathbf{P}(\mathbf{d},T_a)=\frac{\partial\mathcal{W}(\mathbf{F})}{\partial\mathbf{F}}+T_a(\mathbf{s},SL)\frac{\mathbf{F}\mathbf{f}_0\otimes\mathbf{f}_0}{\sqrt{\mathcal{I}_{4f}}}, \tag{6}$$

where the first term stands as the passive part of the tensor $\mathbf{P}$, while the latter as the active one; $\mathcal{W}:\text{Lin}^+\to\mathbb{R}$ is the strain energy density function, $T_a(\mathbf{s},SL)$ is the active tension, provided by the activation model $(\mathscr{A})$.

To model the passive behaviour of cardiac tissue, we employ the orthotropic Guccione constitutive law [25], whose strain energy function is defined as:

$$\mathcal{W}=\frac{\frac{B}{2}(J-1)\log(J)+\bar{C}}{2}\left(e^{Q}-1\right), \tag{7}$$

where the first term is the volumetric energy with bulk modulus B, which penalizes large variations of volume to enforce a weakly incompressible behavior [20,43], and the latter is the deviatoric energy with $\bar{C}$ being the stiffness scaling parameter:

$$\bar{C}=C[\eta+(1-\eta)4.56]. \tag{8}$$

The coefficient C is fitted from experiments [25]. As in cardiac electrophysiology $(\mathscr{E})$, we assign $\eta=1$ to healthy tissue, $\eta\in[0.1,1)$ represents grey zones, and $\eta=0$ defines scar regions. In this way, we model a stiffer myocardium for infarcted areas. Finally, the exponent Q reads:

$$\begin{aligned}Q=&b_{\text{ff}}E_{\text{ff}}^2+b_{\text{ss}}E_{\text{ss}}^2+b_{\text{nn}}E_{\text{nn}}^2+b_{\text{fs}}\left(E_{\text{fs}}^2+E_{\text{sf}}^2\right)+b_{\text{fn}}\left(E_{\text{fn}}^2+E_{\text{nf}}^2\right)\cdot\\&+b_{\text{sn}}\left(E_{\text{sn}}^2+E_{\text{ns}}^2\right),\end{aligned} \tag{9}$$

in which $E_{ij}=\boldsymbol{E}\mathbf{i}_0\cdot\mathbf{j}_0$ for i,j ∈ {f,s,n} are the entries of $\mathbf{E}=\frac{1}{2}(\mathbf{C}-\mathbf{I})$, i.e the Green-Lagrange strain energy tensor, being $\mathbf{C}=\mathbf{F}^T\mathbf{F}$ the right Cauchy-Green deformation tensor.

To model the mechanical effects of the pericardial sac [23,44,64], we impose at the epicardial boundary Γ_0^{epi} a generalized Robin boundary

condition $\mathbf{P}(\mathbf{d},T_a)\mathbf{N}=\mathbf{K}^{epi}\mathbf{d}+\mathbf{C}^{epi}\frac{\partial \mathbf{d}}{\partial t}$ by defining the tensors $\mathbf{K}^{epi}=K_{\parallel}^{epi}(\mathbf{N}\otimes\mathbf{N}-\mathbf{I})-K_{\perp}^{epi}(\mathbf{N}\otimes\mathbf{N})$ and $\mathbf{C}^{epi}=C_{\parallel}^{epi}(\mathbf{N}\otimes\mathbf{N}-\mathbf{I})-C_{\perp}^{epi}(\mathbf{N}\otimes\mathbf{N})$, where $K_{\perp}^{epi}$, $K_{\parallel}^{epi}$, $C_{\perp}^{epi}$, $C_{\parallel}^{epi}\in\mathbb{R}^{+}$ are the stiffness and viscosity parameters of the epicardial tissue in the normal and tangential directions, respectively. Normal stress boundary conditions were imposed at the endocardium of the LV Γ_0^{endo}, in which $p_{LV}(t)$ is the pressure exerted by the blood in the LV, modeled by means of the 0D closed-loop circulation model [56]. To take into account the effect of the neglected part, over the basal plane, on the ventricular domain, we set on Γ_0^{base} the energy consistent boundary condition $\mathbf{P}(\mathbf{d},T_a)\mathbf{N}=|J\mathbf{F}^{-T}\mathbf{N}|\mathbf{v}_{LV}^{base}(t)$ [53], where:

$$\mathbf{v}_{LV}^{base}(t)=\frac{\int_{\Gamma_0^{endo}}p_{LV}(t)J\mathbf{F}^{-T}\mathbf{N}d\Gamma_0}{\int_{\Gamma_0^{base}}|J\mathbf{F}^{-T}\mathbf{N}|d\Gamma_0}. \tag{10}$$

2.1.4. Blood circulation ($\mathscr{C}$) and coupling conditions ($\mathscr{V}$)

We model the blood circulation through the entire cardiovascular system by means of a closed-loop model recently proposed in Ref. [56]. In the 0D closed-loop model, systemic and pulmonary circulations are modeled with RLC circuits, heart chambers are described by time-varying elastance elements and non-ideal diodes stand for the heart valves.

We represent the circulation core model ($\mathscr{C}$) with the following system of ODEs:

$$\begin{cases}
\frac{dV_{LA}(t)}{dt}=Q_{VEN}^{PUL}(t)-Q_{MV}(t), & \frac{dV_{LV}(t)}{dt}=Q_{MV}(t)-Q_{AV}(t),\\
\frac{dV_{RA}(t)}{dt}=Q_{VEN}^{SYS}(t)-Q_{TV}(t), & \frac{dV_{RV}(t)}{dt}=Q_{TV}(t)-Q_{PV}(t),\\
C_{AR}^{SYS}\frac{dp_{AR}^{SYS}(t)}{dt}=Q_{AV}(t)-Q_{AR}^{SYS}(t), & C_{VEN}^{SYS}\frac{dp_{VEN}^{SYS}(t)}{dt}=Q_{AR}^{SYS}(t)-Q_{VEN}^{SYS}(t),\\
C_{AR}^{PUL}\frac{dp_{AR}^{PUL}(t)}{dt}=Q_{PV}(t)-Q_{AR}^{PUL}(t), & C_{VEN}^{PUL}\frac{dp_{VEN}^{PUL}(t)}{dt}=Q_{AR}^{PUL}(t)-Q_{VEN}^{PUL}(t),\\
\frac{L_{AR}^{SYS}}{R_{AR}^{SYS}}\frac{dQ_{AR}^{SYS}(t)}{dt}=-Q_{AR}^{SYS}(t)-\frac{p_{VEN}^{SYS}(t)-p_{AR}^{SYS}(t)}{R_{AR}^{SYS}},\\
\frac{L_{VEN}^{SYS}}{R_{VEN}^{SYS}}\frac{dQ_{VEN}^{SYS}(t)}{dt}=-Q_{VEN}^{SYS}(t)-\frac{p_{RA}(t)-p_{VEN}^{SYS}(t)}{R_{VEN}^{SYS}},\\
\frac{L_{AR}^{PUL}}{R_{AR}^{PUL}}\frac{dQ_{AR}^{PUL}(t)}{dt}=-Q_{AR}^{PUL}(t)-\frac{p_{VEN}^{PUL}(t)-p_{AR}^{PUL}(t)}{R_{AR}^{PUL}},\\
\frac{L_{VEN}^{PUL}}{R_{VEN}^{PUL}}\frac{dQ_{VEN}^{PUL}(t)}{dt}=-Q_{VEN}^{PUL}(t)-\frac{p_{LA}(t)-p_{VEN}^{PUL}(t)}{R_{VEN}^{PUL}},
\end{cases}$$

with $t\in(0,T]$, where:

$$\begin{aligned}
p_{LV}(t)&=p_{EX}(t)+E_{LV}(t)\big(V_{LV}(t)-V_{0,LV}\big),\\
p_{LA}(t)&=p_{EX}(t)+E_{LA}(t)\big(V_{LA}(t)-V_{0,LA}\big),\\
p_{RV}(t)&=p_{EX}(t)+E_{RV}(t)\big(V_{RV}(t)-V_{0,RV}\big),\\
p_{RA}(t)&=p_{EX}(t)+E_{RA}(t)\big(V_{RA}(t)-V_{0,RA}\big),\\
Q_{MV}(t)&=\frac{p_{LA}(t)-p_{LV}(t)}{R_{MV}(p_{LA}(t),p_{LV}(t))}, \qquad Q_{AV}(t)=\frac{p_{LV}(t)-p_{AR}^{SYS}(t)}{R_{AV}(p_{LV}(t),p_{AR}^{SYS}(t))},\\
Q_{TV}(t)&=\frac{p_{RA}(t)-p_{RV}(t)}{R_{TV}(p_{RA}(t),p_{RV}(t))}, \qquad Q_{PV}(t)=\frac{p_{RV}(t)-p_{AR}^{PUL}(t)}{R_{PV}(p_{RV}(t),p_{AR}^{PUL}(t))},
\end{aligned}$$

with $t\in[0,T]$. Here p_{LA}, V_{LA}, p_{RA}, V_{RA}, p_{LV}, V_{LV}, p_{RV} and V_{RV} refer to the pressures and volumes of left atrium, right atrium, left ventricle and right ventricle, respectively; p_{AR}^{SYS}, Q_{AR}^{SYS}, p_{VEN}^{SYS}, Q_{VEN}^{SYS}, p_{AR}^{PUL}, Q_{AR}^{PUL}, p_{VEN}^{PUL} and Q_{VEN}^{PUL} express pressures and flow rates of the systemic and pulmonary circulation (arterial and venous). To couple the 0D circulation model ($\mathscr{C}$) with the 3D LV model, given by ($\mathscr{E}$)–($\mathscr{A}$)–($\mathscr{M}$), we follow the same strategy proposed in Ref. [56]. In particular, we replace the time-varying elastance elements representing the LV in ($\mathscr{C}$) with its corresponding 3D electromechanical description and we introduce the coupling condition:

$$(\mathscr{V})\quad V_{LV}(\boldsymbol{c}(t))=V_{LV}^{3D}(\mathbf{d}(t))\ \text{for}\ t\in(0,T], \tag{11}$$

where:

$$V_{LV}^{3D}(\mathbf{d}(t))=\int_{\Gamma_0^{endo}}J(t)((\mathbf{h}\otimes\mathbf{h})(\mathbf{x}+\mathbf{d}(t)-\mathbf{b}))\cdot\mathbf{F}^{-T}(t)\mathbf{N}\,d\Gamma_0$$

in which $\mathbf{h}$ is a vector orthogonal to the LV centerline (i.e. lying on the ventricular base) and $\mathbf{b}$ lays inside the LV [56].

Due to ($\mathscr{V}$), in the 3D-0D coupled model, $p_{LV}(t)$ is not determined by the 0D circulation model, but rather acts as Lagrange multipliers and enforces the constraint ($\mathscr{V}$).

2.2. Reference configuration

Cardiac geometries are acquired from in vivo medical images through imaging techniques. These geometries are in principle not stress free, mainly because there is always a pressure acting on the endocardium. Therefore, one needs to estimate the unloaded (i.e. stress-free) configuration (also named reference configuration) to which the 3D-0D cardiac electromechanical model refers. To recover the reference configuration Ω_0, starting from a geometry acquired from medical images $\widetilde{\Omega}$, we apply the same procedure proposed for the left ventricle in Ref. [56].

Specifically, we solve an inverse problem: find the solution $\mathbf{d}=\mathbf{d}_{\Omega_0}$ of the following differential problem

$$\begin{cases}
\nabla\cdot\mathbf{P}(\mathbf{d},T_a)=\mathbf{0} & \text{in } \Omega_0,\\
\mathbf{P}(\mathbf{d},T_a)\mathbf{N}+\mathbf{K}^{epi}\mathbf{d}=\mathbf{0} & \text{on } \Gamma_0^{epi},\\
\mathbf{P}(\mathbf{d},T_a)\mathbf{N}=-p_{LV}(t)\,J\mathbf{F}^{-T}\mathbf{N} & \text{on } \Gamma_0^{endo},\\
\mathbf{P}(\mathbf{d},T_a)\mathbf{N}=|J\mathbf{F}^{-T}\mathbf{N}|\mathbf{v}_{LV}^{base}(t) & \text{on } \Gamma_0^{base},
\end{cases} \tag{12}$$

obtained for $p_{LV}=\widetilde{p}_{LV}$ and $T_a=\widetilde{T}_a$, such that we get the domain $\widetilde{\Omega}=\{\mathbf{x}:\mathbf{x}=\mathbf{x}_0+\mathbf{d}\ \ \forall\mathbf{x}_0\in\Omega_0\}$.

Finally, to properly initialize the numerical simulation, we inflate the ventricular reference configuration Ω_0 by solving problem (12), where we set the pressures $p_{LV}=p_{LV}^{ED}$. The value p_{LV}^{ED} is chosen to bring the left ventricle to a defined volume V_{LV}^{ED}, as explained in Ref. [46]. Then, the solution $\mathbf{d}$ of the problem (12) is set as initial condition $\mathbf{d}_0$ for $\mathbf{d}$ (with $\dot{\mathbf{d}}_0=\mathbf{0}$) in ($\mathscr{M}$).

3. Numerical methods

We adopt the geometric model of the Zygote LV depicted in Fig. 2. We consider an idealized distribution of ischemic regions, which is made by two scars and two different types of grey zones.

To generate the fibers distribution (field $\mathbf{f}_0$) for our geometry, we use the Bayer-Blake-Plank-Trayanova algorithm [7,45] with $\alpha_{epi}=-60^{\circ}$, $\alpha_{endo}=60^{\circ}$, $\beta_{epi}=20^{\circ}$, and $\beta_{endo}=-20^{\circ}$.

We employ the strategy proposed in Ref. [54] to choose proper initial conditions for the 3D electromechanical simulations, by relying on a 0D

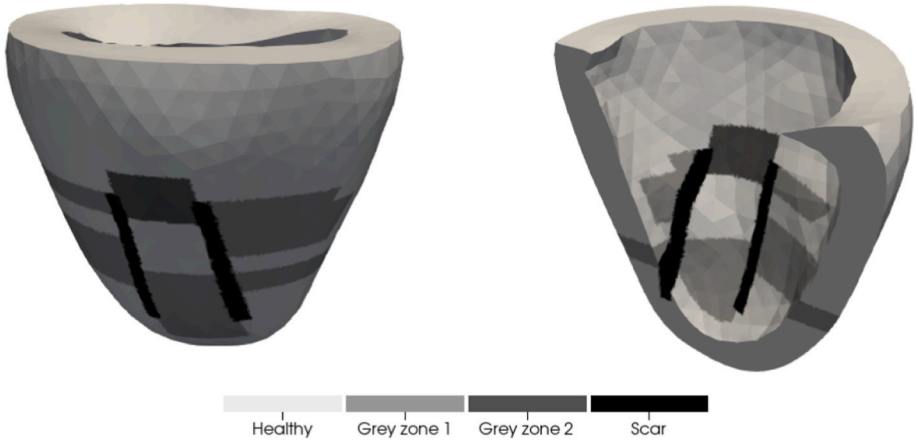

Fig. 2. Zygote LV with the idealized distribution of scars (black), grey zones (grey) and non-remodeled regions (white) over the myocardium. Volumetric view (left) and cut view (right). The first type of grey zone corresponds to $\eta = 0.2$, while on the second one $\eta = 0.1$ is prescribed.

emulator. In particular, to reach a steady state for the electrophysiological variables, we trigger periodic stimuli with a period equal to 0.45 s, for a total duration of 450 s. On the other hand, for the 3D numerical simulations, we apply an S1–S2 stimulation protocol consisting of two gaussian stimuli, the first one applied at time $t = 0$ s and the second one applied at time $t = 0.45$ s. In this way the 3D electromechanical simulations are a natural continuation of the 0D initialization, and the VT can be directly induced by just using a single S1 before the S2.

We use a segregated-intergrid-staggered scheme to numerically discretize the electromechanical model [46]. Indeed, we solve $(\mathscr{E})$, $(\mathscr{A})$, $(\mathscr{M}) - (\mathscr{V})$ and $(\mathscr{C})$ sequentially, by employing different time and space resolutions according to the specific core model.

We employ the Finite Element Method (FEM) for the space discretization of electrophysiological, activation and mechanical models [48,49]. We use hexahedral meshes and $\mathbb{Q}_1$ finite element spaces for the space discretization of all the core models. This multiphysics problem presents different space resolutions according to the specific model at hand [56,57]. In the framework of cardiac electrophysiology, we consider a fine geometrical description (1′987′285 DOFs, 1′926′912 cells, $h_{\text{mean}} \approx 0.86$ mm) to accurately capture the electric propagation due to fine-scale phenomena arising from the continuum modeling of the cellular level, especially with the aim of reproducing and properly address arrhythmias [61]. On the other hand, cardiac mechanics allows a lower space resolution (35′725 DOFs, 30′108 cells, $h_{\text{mean}} \approx 3.3$ mm). This eases its numerical solution, which is computationally demanding, especially for the assembling phase [61]. Differently from Ref. [62], in this paper we consider a significant space scales separation between electrophysiology and mechanics because we are dealing with a simple distribution of ischemic regions.

For time discretization, we use backward differentiation formula (BDF) schemes [48]. In particular, we employ a third order BDF scheme for electrophysiology and a first order BDF scheme for activation, mechanics and circulation. These choices allow to accurately capture the fast time dynamics of the model variables without unbearable restrictions on the time step, while not introducing numerical instabilities. We treat the nonlinear terms coming from both electrophysiological and activation models in a semi-implicit fashion. Cardiac mechanics is numerically advanced in time with a fully implicit scheme. The cardiocirculatory model is solved with an explicit method [46]. To stabilize the numerical oscillations arising from the feedback of the tissue mechanics on the activation model, without having to resort to a monolithic strategy, we rely on the scheme proposed in Ref. [55]. We use a smaller time step for electrophysiology ($\tau = 50$ μs) than for activation, mechanics and circulation ($\Delta t = 500$ μs). We set the final time $T = 4$ s for all the numerical simulations.

The mathematical models of Section 2 and the numerical methods presented in this section have been implemented in `lifex` (https://lifex.gitlab.io/lifex), a high-performance `C++` library developed within the iHEART project and based on the `deal.II` (https://www.dealii.org) Finite Element core [2].

The numerical simulations were performed on a HPC facility available at MOX for the iHEART project. The entire cluster is endowed with 8 Intel Xeon Platinum 8160 processors, for a total of 192 computational cores and a total amount of 1.5 TB of available RAM.

4. Numerical results

We present electromechanical simulations to evaluate the effects of MEFs. We consider different modeling choices for the monodomain equation, as reported in Table 1. We start from a baseline simulation with model $(\mathscr{E})$, in which we obtain a stable VT. Then, we compare the effects of different geometry-mediated MEFs, i.e. models $(\mathscr{E})$, $(\mathscr{E}_{\text{gMEF-minimal}})$, $(\mathscr{E}_{\text{gMEF-enhanced}})$ and $(\mathscr{E}_{\text{gMEF-full}})$. We also study the impact of different parametrizations for SACs, i.e. $(\mathscr{E}_{\text{SAC}})$, with respect to $(\mathscr{E})$. Finally, we evaluate the combined effects of geometry-mediated MEFs and nonselective SACs. We report in Appendix A the values of the parameters to perform the numerical simulations that will be discussed in this paper.

4.1. Baseline simulation

We depict in Fig. 3 the evolution of the transmembrane potential and the displacement magnitude for the baseline electromechanical simulation, where all MEFs are fully neglected (model $(\mathscr{E})$ in Table 1). We induce a sustained VT with a figure-of-eight pattern around the isthmus, which is laterally bordered by scars, that act as conduction blocks [22].

In Fig. 4, we compare the Pressure-Volume (PV) loop over different heartbeats for the baseline simulation under VT with a reference healthy

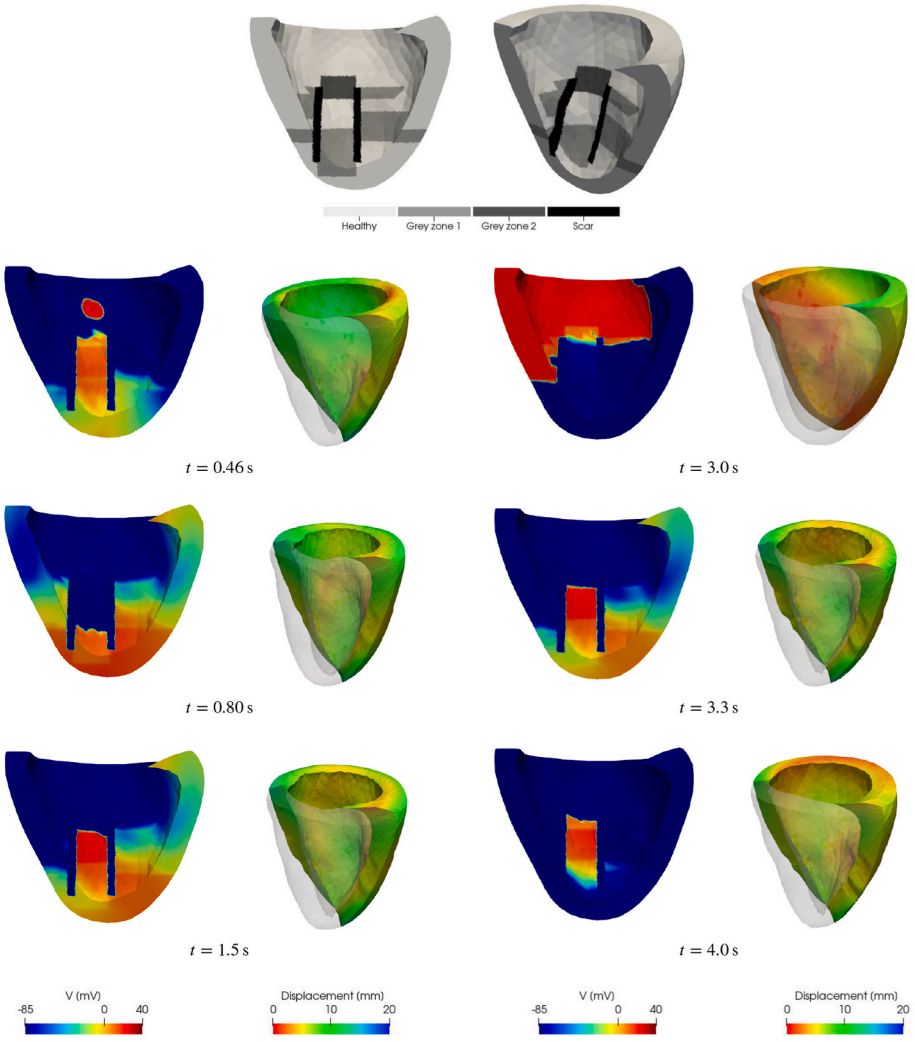

Fig. 3. Time evolution of the transmembrane potential V (left) and displacement magnitude $|\mathbf{d}|$ (right) for the Zygote LV with an idealized distribution of ischemic regions. Each picture on the right side is warped by the displacement vector $\mathbf{d}$. MEFs are neglected, i.e. we use model ($\mathscr{E}$).

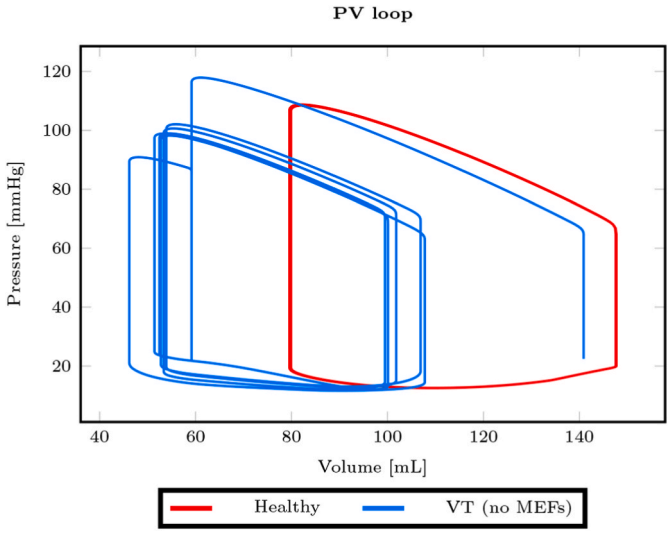

Fig. 4. Comparison between a reference healthy PV loop in sinus rhythm (red, Appendix A, heartbeat period equal to 0.8 s) and the one obtained in the baseline simulation under VT for $t \in [0, 4]$ s (light blue). We underline that, differently from Ref. [62], here we induce a hemodynamically tolerated VT. (For interpretation of the references to colour in this figure legend, the reader is referred to the Web version of this article.)

PV loop in sinus rhythm obtained by removing scars and grey zones. We observe that the contractility increases while the stroke volume (SV) decreases. The ejection fraction (EF) remains approximately the same and we approach a steady state in which the electromechanical function is not impaired. For these reasons, we conclude that the VT is stable.

VT associated with ischemia are known to disturb the normal isovolumetric processes and to influence the end systolic/diastolic pressure volume relationship (ESPVR/EDPVR) [6]. Simultaneously, a phenomenon called incomplete relaxation may occur, especially when the VT does not leave enough time for the uncoupling of all the actin-myosin bonds between two consecutive contraction phases [6]. The occurrence of this phenomenon is illustrated in Fig. 5, where we depict the time evolution of the minimum, maximum and average active stress in the computational domain Ω_0 for a reference healthy case in sinus rhythm and the baseline simulation under VT. Specifically, in the healthy case there is always a time interval between two consecutive heartbeats (precisely, during ventricular diastole) in which the active stress is virtually zero in the LV. In the VT case, instead, the cardiac muscle is never fully relaxed, thus not allowing the LV to complete its emptying. All these details are properly captured by our electromechanical model thanks to its biophysical accuracy.

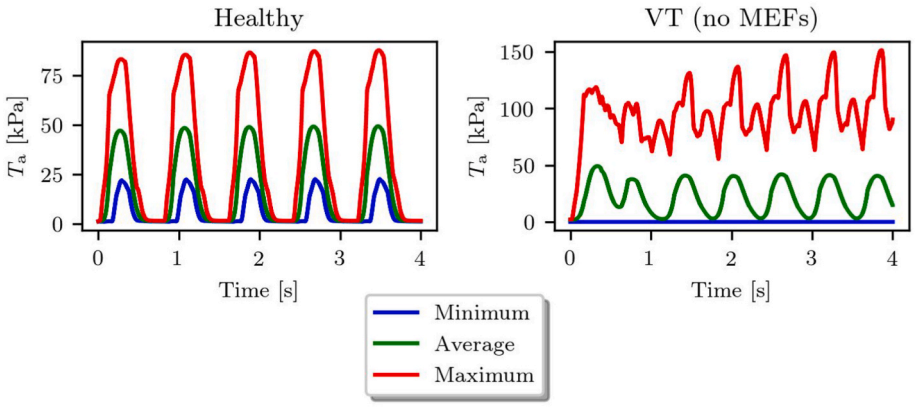

Fig. 5. Minimum, average and maximum active tension T_a over time for a reference healthy case in sinus rhythm (left, Appendix A, heartbeat period equal to 0.8 s) and the baseline simulation under VT (right). We see that incomplete relaxation occurs during VT.

4.2. *Effects of geometry-mediated MEFs*

We consider four different modeling choices for the geometry-mediated MEFs, namely $(\mathscr{E})$, $(\mathscr{E}_{\text{gMEF}-\text{minimal}})$, $(\mathscr{E}_{\text{gMEF}-\text{enhanced}})$ and $(\mathscr{E}_{\text{gMEF}-\text{full}})$ in Table 1, while for the moment we completely neglect the impact of SACs. Then, we perform four different electromechanical simulations by employing these four different formulations for the monodomain equation.

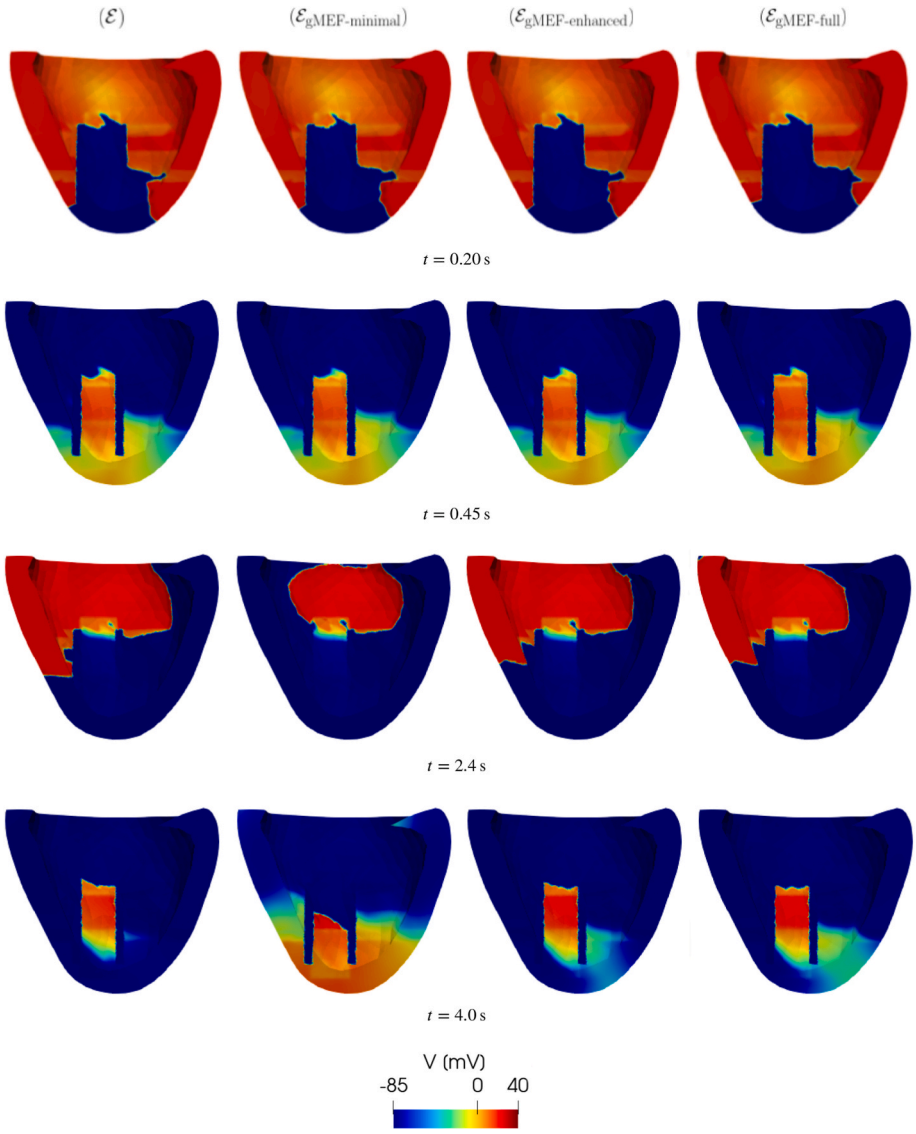

Fig. 6. Comparison among different models for geometry-mediated MEFs in terms of transmembrane potential V.

Table 2
BCL for different modeling choices in geometry-mediated MEFs. Model $(\mathscr{E}_{\text{gMEF-minimal}})$ significantly changes BCL with respect to $(\mathscr{E})$, $(\mathscr{E}_{\text{gMEF-enhanced}})$, $(\mathscr{E}_{\text{gMEF-full}})$.

Model	$(\mathscr{E})$	$(\mathscr{E}_{\text{gMEF-minimal}})$	$(\mathscr{E}_{\text{gMEF-enhanced}})$	$(\mathscr{E}_{\text{gMEF-full}})$
BCL	0.60 s	0.65 s	0.61 s	0.60 s

We illustrate in Fig. 6 the development of transmembrane potential V over time. We observe minor differences in the propagation of the transmembrane potential among $(\mathscr{E})$, $(\mathscr{E}_{\text{gMEF-enhanced}})$ and $(\mathscr{E}_{\text{gMEF-full}})$. These differences, as we can see for $t = 4$ s, are mainly focused on the depolarization wave and occur during VT. Moreover, by looking at Table 2, we notice that the VT basis cycle length (BCL) is very similar among these three models. Indeed, the BCL is approximately equal to 0.60 s, which is long if compared to more dangerous VT and justifies a stable ventricular excitation.

On the other hand, $(\mathscr{E}_{\text{gMEF-minimal}})$ entails major changes in VT BCL, which increases from 0.60 s (for model $(\mathscr{E})$) to 0.65 s, and conduction velocity, that significantly decreases.

These observations are in agreement with Fig. 7, where the electrophysiological, mechanical and hemodynamic variables retrieved in a random point of the computational domain are shifted forward for $(\mathscr{E}_{\text{gMEF-minimal}})$, while $(\mathscr{E})$, $(\mathscr{E}_{\text{gMEF-enhanced}})$ and $(\mathscr{E}_{\text{gMEF-full}})$ show a very similar pattern. This is also motivated by the change in the VT exit site, as we can see from Fig. 6 for $t = 2.4$ s. This phenomenon is particularly evident from the plot of sarcomere length over time (Fig. 7), which also presents different peak values for $(\mathscr{E}_{\text{gMEF-minimal}})$ and $t \gtrapprox 2.4$ s. Finally, we see that wavefront stability is not affected by geometry-mediated MEFs. The VT always remains hemodynamically stable in the four different cases.

4.3. Effects of SACs

In this section, we fully neglect the effects of geometry-mediated MEFs and we focus on different parametrizations for SACs in terms of G_s and V_{rev}. We also compare the outcomes of $(\mathscr{E}_{\text{SAC}})$ with the ones of $(\mathscr{E})$ to outline similarities and differences.

We notice from Fig. 8 that both APD and wavefront stability are

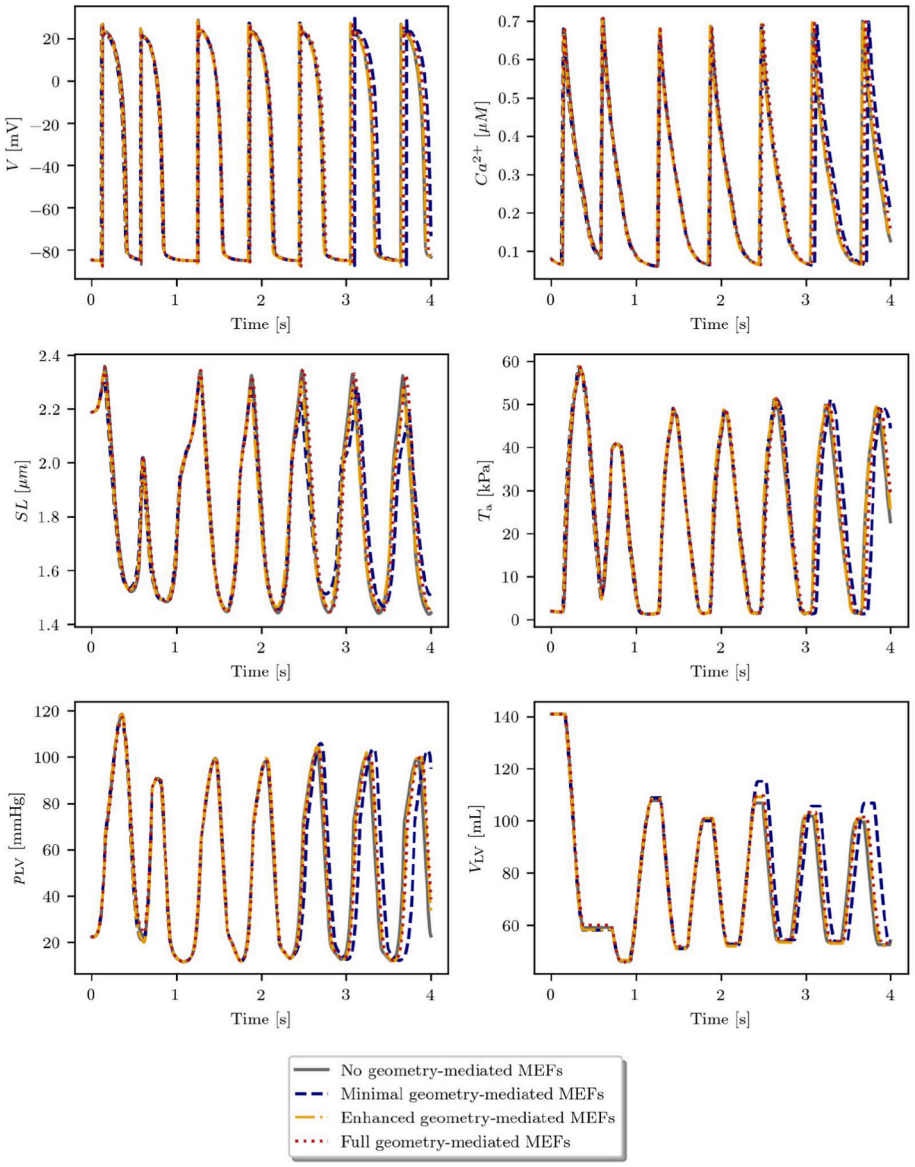

Fig. 7. Pointwise values of transmembrane potential V, intracellular calcium concentration $[Ca^{2+}]_i$, sarcomere length SL, active tension T_a, pressure p_{LV} and volume V_{LV} over time for $(\mathscr{E})$, $(\mathscr{E}_{\text{gMEF-minimal}})$, $(\mathscr{E}_{\text{gMEF-enhanced}})$ and $(\mathscr{E}_{\text{gMEF-full}})$.

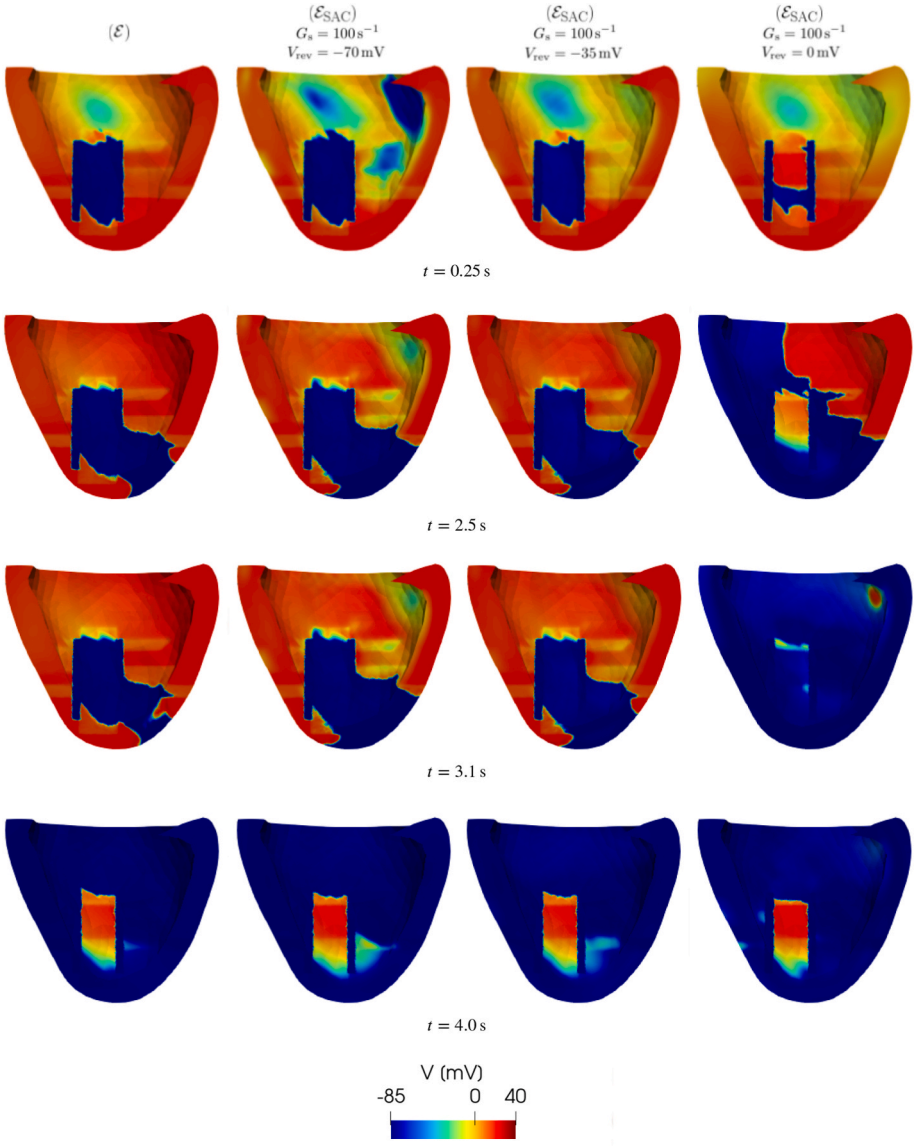

Fig. 8. Comparison between model ($\mathscr{E}$) and model ($\mathscr{E}_{\mathrm{SAC}}$), for different values of V_{rev} ($G_s = 100\ \mathrm{s}^{-1}$).

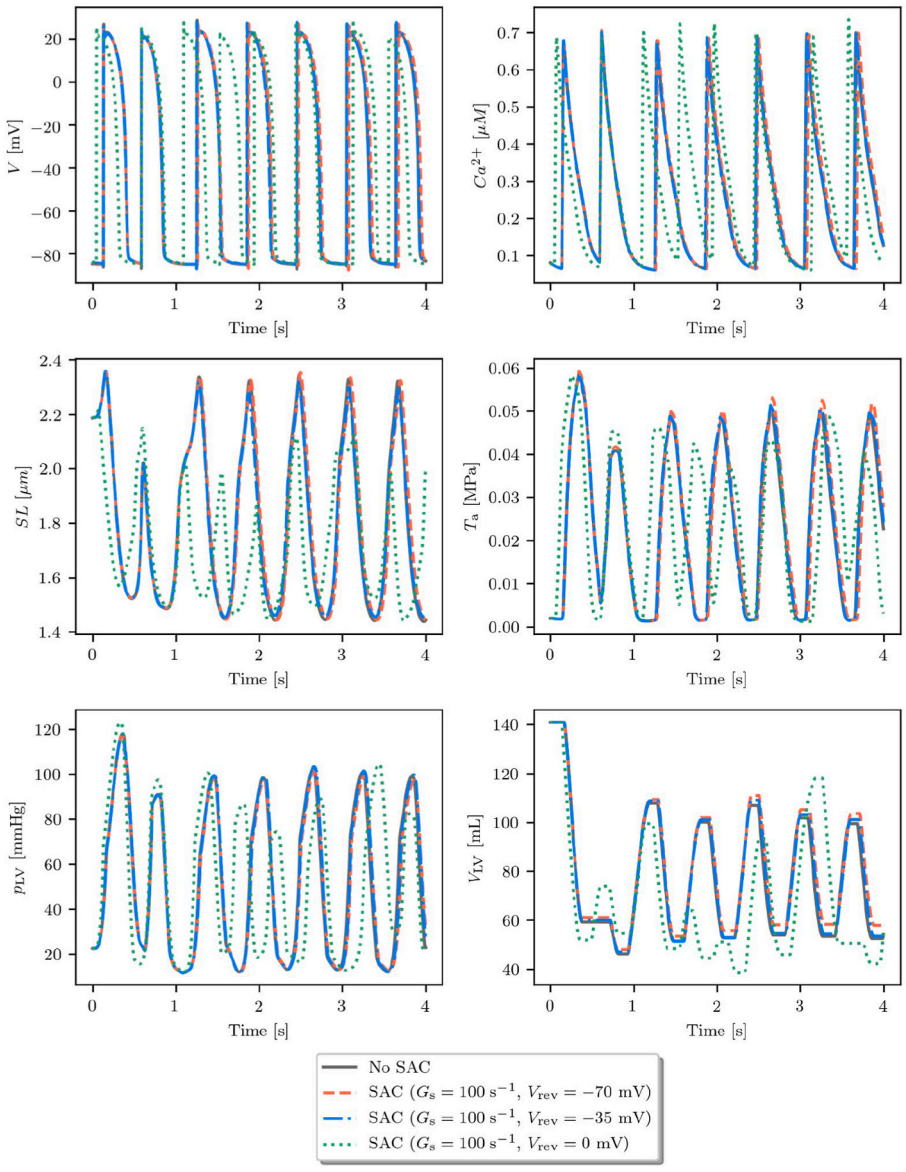

Fig. 9. Pointwise values of transmembrane potential V, intracellular calcium concentration $[Ca^{2+}]_i$, sarcomere length SL, active tension T_a, pressure p_{LV} and volume V_{LV} over time for ($\mathscr{E}$) and ($\mathscr{E}_{SAC}$) with different choices of V_{rev} ($G_s = 100\ s^{-1}$).

Table 3
VT classification for different SACs parametrizations. The unstable VT has a BCL that ranges from 0.43 s to 0.58 s.

Model	VT type
$(\mathscr{E})$	Stable (BCL = 0.60 s)
$(\mathscr{E}_{\text{SAC}})$, $G_s = 100\ \text{s}^{-1}$, $V_{\text{rev}} = -70$ mV	Stable (BCL = 0.60 s)
$(\mathscr{E}_{\text{SAC}})$, $G_s = 100\ \text{s}^{-1}$, $V_{\text{rev}} = -35$ mV	Stable (BCL = 0.60 s)
$(\mathscr{E}_{\text{SAC}})$, $G_s = 100\ \text{s}^{-1}$, $V_{\text{rev}} = 0$ mV	Unstable ($\text{BCL}_{\text{avg}} = 0.50$ s)
$(\mathscr{E}_{\text{SAC}})$, $G_s = 50\ \text{s}^{-1}$, $V_{\text{rev}} = 0$ mV	Stable (BCL = 0.60 s)

affected by SACs parametrizations. Indeed, by combining the 3D information with the pointwise evaluations of Fig. 9, we discover that there is one choice of the parameters, namely $G_s = 100\ \text{s}^{-1}$ and $V_{\text{rev}} = 0$ mV, that converts the VT from stable to unstable. The instability derives from an extra stimulus that is completely driven by contraction, which occurs in the superior-right part of the ventricle. This extra stimulus changes the reentrant circuit, along with its BCL, which is not the same over time.

By considering data of Table 3, we observe that the VT BCL remains the same when there is no stability transition. Moreover, from the hemodynamic perspective, the onset of different types of arrhythmias is driven by the combined effects of G_s and V_{rev}. Indeed, in Fig. 9 we see that given G_s, different V_{rev} may change wavefront stability. On the other hand, in Fig. 10 we show that different G_s may affect wavefront stability, with V_{rev} fixed a priori.

4.4. Combined effects of geometry-mediated MEFs and SACs

We briefly evaluate the combined effects of geometry-mediated MEFs and nonselective SACs. Once SACs parametrization is fixed, we notice that switching between no formulation (i.e. $(\mathscr{E}_{\text{SAC}})$) to full formulation (i.e. $(\mathscr{E}_{\text{gMEF-full, SAC}})$) of geometry-mediated MEFs entails significant differences. In particular, from Fig. 11 we see that $(\mathscr{E}_{\text{gMEF-full, SAC}})$ triggers the extra stimuli faster than $(\mathscr{E}_{\text{SAC}})$.

As we can notice from Fig. 12, the VT remains unstable but both pressure and volume traces over time are very different from each other for $(\mathscr{E}_{\text{SAC}})$ and $(\mathscr{E}_{\text{gMEF-full, SAC}})$.

From Table 4, we infer that the VT BCL for $(\mathscr{E}_{\text{gMEF-full, SAC}})$ is lower than the one of $(\mathscr{E}_{\text{SAC}})$. This potentially defines a more dangerous VT.

Finally, in Fig. 13 we highlight the joint contributions of electrophysiology, mechanics and hemodynamics in the $(\mathscr{E}_{\text{gMEF-full, SAC}})$ coupled model.

5. Discussion

We investigate how several types of geometry-mediated MEFs and different parametrizations for nonselective SACs affect the electric and hemodynamic stability of VT. In particular, we focus on the electric properties of VT macro-reentrant circuits and we analyze the modifications on blood supply by means of PV loops.

Differently from previous studies [13,32,67], we keep into account tissue heterogeneity by introducing an idealized distribution of scars, grey zones and non-remodeled regions over the myocardium. We also consider a more sophisticated coupled mathematical model that embraces electrophysiology, activation, mechanics and cardiovascular fluid dynamics to analyze these mechano-electric couplings. To the best of our knowledge, this framework enables to study for the first time the hemodynamic effects of both geometry-mediated MEFs and nonselective SACs on VT by means of electromechanical simulations, showing strengths and weaknesses of some simplifying modeling choices that are commonly made when simulating this type of phenomenon [11,15,37,50]. The coupling between the 3D electromechanical model and the 0D circulation model permits to identify the hemodynamic nature of the VT. With our approach, we discriminate between stable and unstable VT, which might result in hemodynamically tolerated or not tolerated VT [62].

We see that if a VT is triggered by a certain stimulation protocol and by neglecting all MEFs, the very same pacing protocol induces a VT for all possible combinations of MEFs [62].

In our numerical simulations, we do not observe a significant impact of geometry-mediated MEFs on the induction and sustainment of the VT. Most of the modeling choices for geometry-mediated MEFs, namely $(\mathscr{E})$, $(\mathscr{E}_{\text{gMEF-enhanced}})$ and $(\mathscr{E}_{\text{gMEF-full}})$, present very similar VT BCLs and conduction velocities, while showing a few differences in the depolarization wave [13]. On the other hand, $(\mathscr{E}_{\text{gMEF-minimal}})$ manifests major differences in the VT BCL, which increases, and its exit site with respect to $(\mathscr{E})$, $(\mathscr{E}_{\text{gMEF-enhanced}})$ and $(\mathscr{E}_{\text{gMEF-full}})$, as shown in Ref. [62] for a patient-specific unstable VT. This can be justified by the simplifications introduced in $(\mathscr{E}_{\text{gMEF-minimal}})$, while moving towards $(\mathscr{E}_{\text{gMEF-full}})$ we

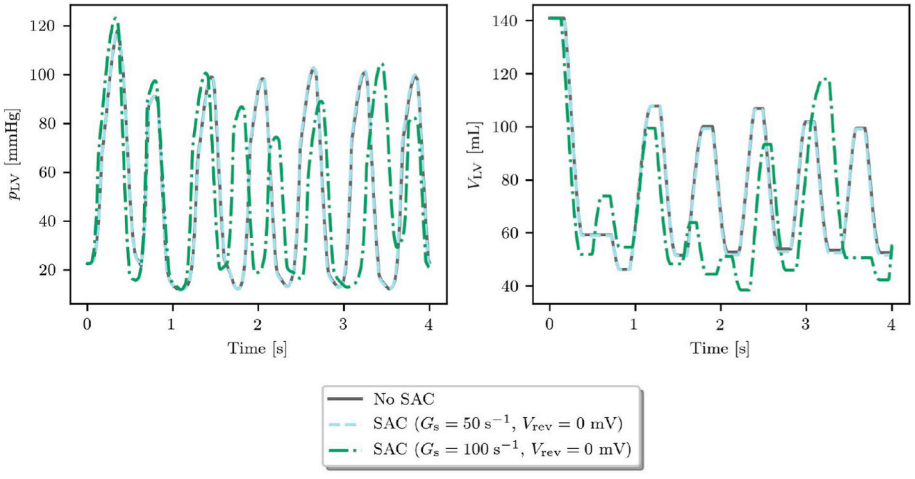

Fig. 10. Pointwise values of pressure p_{LV} and volume V_{LV} over time for $(\mathscr{E})$ and $(\mathscr{E}_{\text{SAC}})$ with different choices of G_s ($V_{\text{rev}} = 0$ mV).

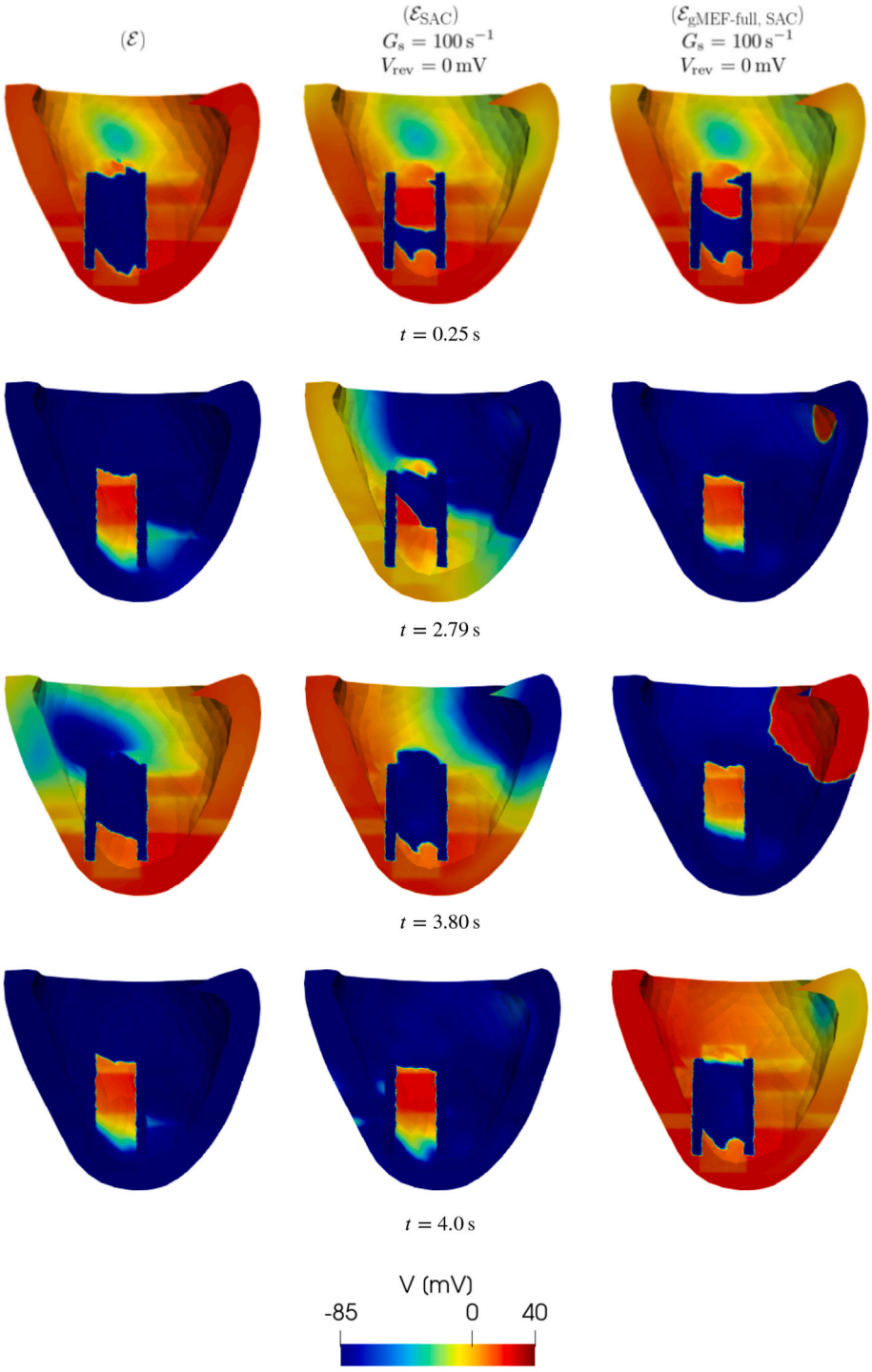

Fig. 11. Comparison among models ($\mathscr{E}$), ($\mathscr{E}_{\text{SAC}}$) and ($\mathscr{E}_{\text{gMEF-full, SAC}}$).

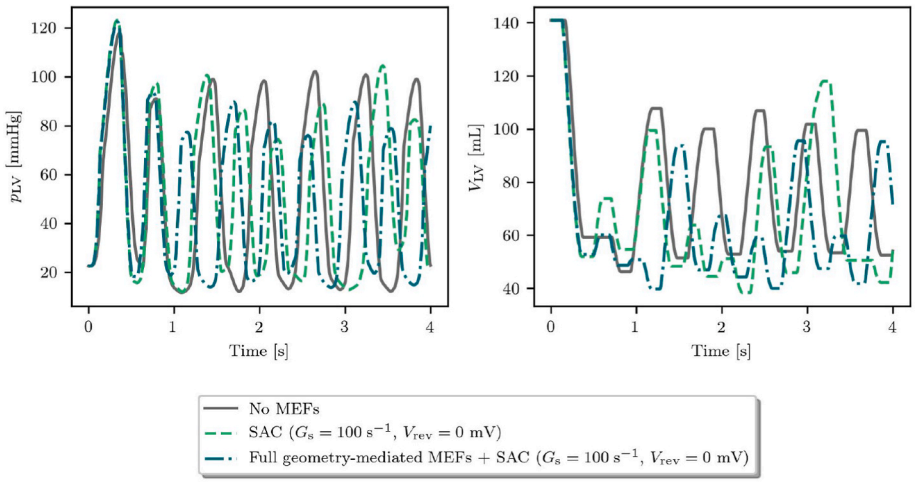

Fig. 12. Pointwise values of pressure p_{LV} and volume V_{LV} over time for $(\mathscr{E})$, $(\mathscr{E}_{SAC})$ ($G_s = 100\ s^{-1}$, $V_{rev} = 0$ mV) and $(\mathscr{E}_{gMEF-full,\ SAC})$ ($G_s = 100\ s^{-1}$, $V_{rev} = 0$ mV).

Table 4
VT classification for combinations of geometry-mediated MEFs and nonselective SACs. The unstable VT related to $(\mathscr{E}_{SAC})$ has a BCL that ranges from 0.43 s to 0.58 s. The unstable VT related to $(\mathscr{E}_{gMEF-full,\ SAC})$ has a BCL that ranges from 0.44 s to 0.50 s.

Model	VT type
$(\mathscr{E})$	Stable (0.60 s)
$(\mathscr{E}_{SAC})$, $G_s = 100\ s^{-1}$, $V_{rev} = 0$ mV	Unstable ($BCL_{avg} = 0.50$ s)
$(\mathscr{E}_{gMEF-full,\ SAC})$, $G_s = 100\ s^{-1}$, $V_{rev} = 0$ mV	Unstable ($BCL_{avg} = 0.47$ s)

almost totally recover the behavior observed in $(\mathscr{E})$. Therefore, the minimal MEFs modeling choice might lead to biased results which are in favor of less severe VT.

We observe that nonselective SACs may affect the hemodynamic nature of the VT, as they may induce EADs or DADs, which lead to ectopic foci that reactivate the LV [26]. These extra stimuli are generally located in the regions of the myocardium in which there is a transition between scar and border zone or between border zone and non-remodeled areas, where high stretches are likely to be present [30]. According to the specific combination of G_s and V_{rev}, nonselective SACs affects both APD and AP resting values [70]. We remark that such spontaneous arrhythmias triggered by myocardial stretches cannot be assessed in electrophysiological simulations, where the mechanical behavior is neglected.

Finally, in our study we also investigate the combined effects of geometry-mediated MEFs and nonselective SACs. Significant differences between $(\mathscr{E}_{gMEF,\ full,\ SAC})$ and $(\mathscr{E}_{SAC})$ are observed when geometry-mediated MEFs are combined with a parametrization of SACs that entails extra stimuli. Specifically, the VT BCL with $(\mathscr{E}_{gMEF,\ full,\ SAC})$ is lower than the one of $(\mathscr{E}_{SAC})$ because the extra stimuli driven by SACs is triggered more often in the former case. This completely changes the pressure-volume dynamics of the VT, whose stability is however still not affected by the geometry-mediated MEFs.

6. Limitations

There are other types of MEFs that could be investigated in future works. Among them, an important role is certainly played by the mechanical effects mediated by fibroblasts in the extracellular matrix, $[Ca^{2+}]_i$ buffers handling, alterations in transmembrane capacitance C_m due to local stretch and ions selective SACs [34]. Indeed, modeling different cellular processes in cardiac electrophysiology might be of interest to further shed light on the underlying mechanisms of arrhythmias. Nevertheless, we have provided a broad study of geometry-mediated MEFs and nonselective SACs by combining electrophysiological, mechanical and hemodynamic observations.

Furthermore, MEFs should be properly quantified in patient-specific cases. Currently, our model for nonselective SACs permits to put one single value of both G_s and u_{rev} for the whole geometry, which is unlikely to happen in realistic scenarios. A precise space assessment of SACs combined with our mathematical framework could have significant clinical implications.

Finally, we observe that in this work we limited ourselves to the case of transmural scars. We are aware that the clinical practice indicates that most scars are non transmural. Indeed, this is a scenario that we plan to simulate and better analyze in future computational studies. Nevertheless, we expect the analysis conducted on the impact of MEFs on VT to be similar even in the presence of non transmural scars.

7. Conclusions

We studied the effects of geometry-mediated MEFs and nonselective SACs on a realistic LV geometry endowed with an idealized distribution of infarct and peri-infarct zones. We performed numerical simulations of cardiac electromechanics coupled with closed-loop cardiovascular circulation under VT.

Our electromechanical framework allows for the hemodynamic classification of the VT, which can be either stable or unstable, and permits to capture mechanically relevant indications under VT, such as the incomplete relaxation of sarcomeres. Furthermore, by combining

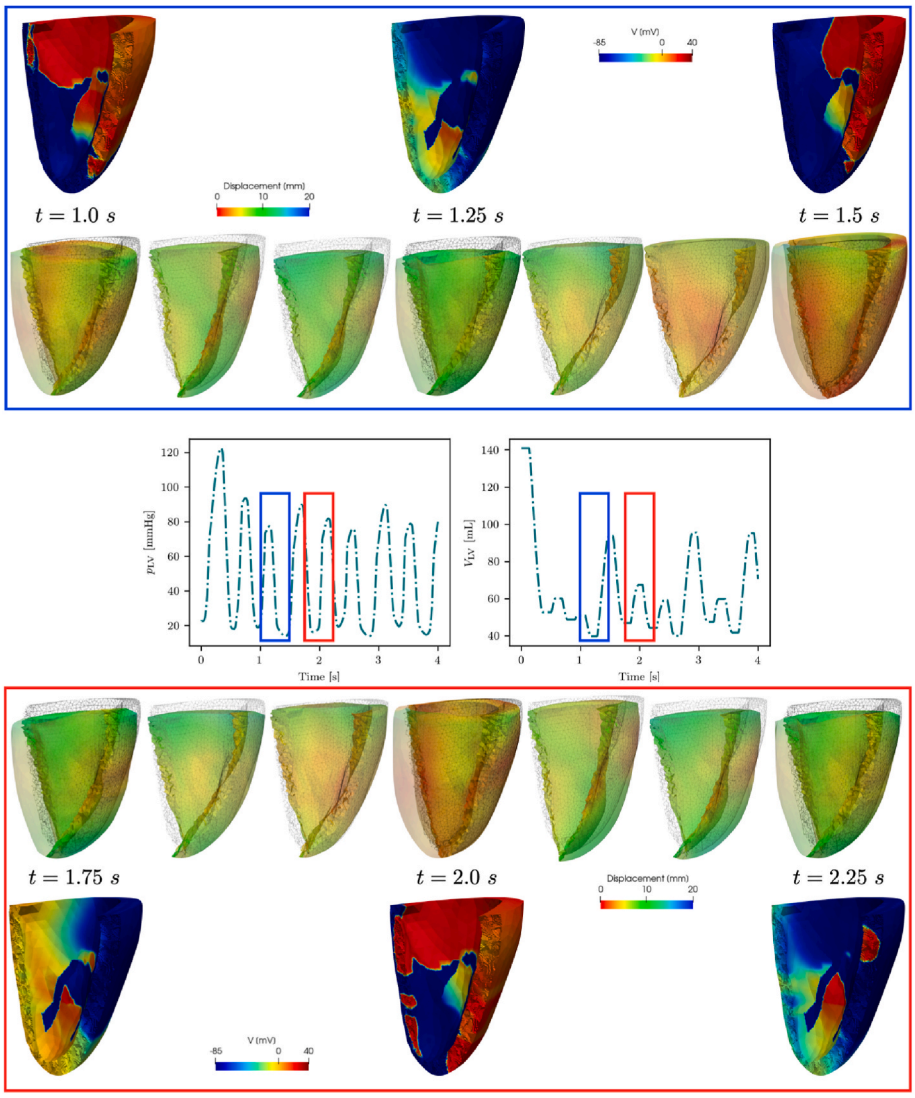

Fig. 13. Coupled effects of electrophysiology, mechanics and hemodynamics for the numerical simulation with model ($\mathscr{E}_{\text{gMEF-full, SAC}}$). The extra stimuli in the upper right part of the LV, which is driven by SACs, activate the LV electrophysiologically and mechanically. This has a direct impact on both pressure and volume transients, which in turn have an effect on the electromechanical behavior of the LV.

electrophysiology, activation, mechanics and hemodynamics, we observed several differences on the VT reentrant circuits dynamics. In particular, geometry-mediated MEFs do not affect VT stability but may alter the VT BCL, along with its exit site [32]. On the other hand, the recruitment of SACs may generate extra stimuli, which may change VT stability. These extra stimuli are driven by myocardial contraction and are induced by changes in the APD or in the resting value of the transmembrane potential [30]. We conclude that both geometry-mediated MEFs and nonselective SACs define important contributions in electromechanical models with hemodynamic coupling, especially when numerical simulations under arrhythmia are carried out.

Declaration of competing interest

The authors declare no conflict of interest.

Acknowledgements

This project has received funding from the European Research Council (ERC) under the European Union's Horizon 2020 research and innovation programme (grant agreement No 740132, iHEART - An Integrated Heart Model for the simulation of the cardiac function, P.I. Prof. A. Quarteroni).

Appendices.

A Model parameters

We provide the full list of parameters adopted for the numerical simulations of this paper. Specifically, Table 5 contains the parameters related to the electrophysiological model, Table 6 those related to the sarcomere model RDQ20-MF, Table 7 the parameters of the mechanical model and, finally, Table 8 contains the parameters associated with the circulation model. For the TTP06 model, we adopt the parameters reported in the original paper (for endocardial cells) [66], with the only difference that we rescale the intracellular calcium concentration $[Ca^{2+}]_i$ by a factor of ω_{Ca} to get more

physiological values [16].

Table 5
Parameters of the electrophysiological model.

Variable	Value	Unit	Variable	Value	Unit
Conductivity tensor			**Applied current**		
σ_{l}	0.76×10^{-4}	$\mathrm{m^2 s^{-1}}$	$\widetilde{\mathcal{I}}_{\mathrm{app}}^{\mathrm{max}}$	17	$\mathrm{V\ s^{-1}}$
σ_{t}	0.35×10^{-4}	$\mathrm{m^2 s^{-1}}$	t_{app}	3e-3	s
σ_{n}	0.11×10^{-4}	$\mathrm{m^2 s^{-1}}$	**Calcium rescaling**		
			ω_{Ca}	0.48	–

Table 6
Parameters of the sarcomere model RDQ20-MF (for the definition of the parameters, see Ref. [52]).

Variable	Value	Unit	Variable	Value	Unit
Regulatory units steady-state			**Crossbridge cycling**		
μ	10	–	$\mu_{f_{\mathcal{P}}}^{0}$	32.255	$\mathrm{s^{-1}}$
γ	30	–	$\mu_{f_{\mathcal{P}}}^{1}$	0.768	$\mathrm{s^{-1}}$
Q	2	–	r_0	134.31	$\mathrm{s^{-1}}$
k_{d}	0.4	μM	α	25.184	–
$\alpha_{k_{\mathrm{d}}}$	−0.208 3	$\mathrm{\mu M\ \mu m^{-1}}$	**Upscaling**		
Regulatory units kinetics			α_{XB}	160	MPa
k_{off}	40	$\mathrm{s^{-1}}$	SL_0	1.9	μm
k_{basic}	8	$\mathrm{s^{-1}}$			

Table 7
Parameters of the mechanical model.

Variable	Value	Unit	Variable	Value	Unit
Constitutive law			**Boundary conditions**		
B	50×10^3	Pa	$K_{\perp}^{\mathrm{epi}}$	2×10^5	$\mathrm{Pa\ m^{-1}}$
C	0.88×10^3	Pa	$K_{\parallel}^{\mathrm{epi}}$	2×10^4	$\mathrm{Pa\ m^{-1}}$
b_{ff}	8	–	$C_{\perp}^{\mathrm{epi}}$	2×10^4	$\mathrm{Pa\ s\ m^{-1}}$
b_{ss}	6	–	$C_{\parallel}^{\mathrm{epi}}$	2×10^3	$\mathrm{Pa\ s\ m^{-1}}$
b_{nn}	3	–	**Tissue density**		
b_{fs}	12	–	ρ_{s}	10^3	$\mathrm{kg\ m^{-3}}$
b_{fn}	3	–			
b_{sn}	3	–			

Table 8
Parameters of the circulation model.

Variable	Value	Unit	Variable	Value	Unit
External circulation			**Cardiac chambers**		
$R_{\mathrm{AR}}^{\mathrm{SYS}}$	0.64	$\mathrm{mmHg\ s\ mL^{-1}}$	$E_{\mathrm{LA}}^{\mathrm{pass}}$	0.18	$\mathrm{mmHg\ mL^{-1}}$
$R_{\mathrm{AR}}^{\mathrm{PUL}}$	0.032 116	$\mathrm{mmHg\ s\ mL^{-1}}$	$E_{\mathrm{RA}}^{\mathrm{pass}}$	0.07	$\mathrm{mmHg\ mL^{-1}}$
$R_{\mathrm{VEN}}^{\mathrm{SYS}}$	0.32	$\mathrm{mmHg\ s\ mL^{-1}}$	$E_{\mathrm{RV}}^{\mathrm{pass}}$	0.05	$\mathrm{mmHg\ mL^{-1}}$
$R_{\mathrm{VEN}}^{\mathrm{PUL}}$	0.035 684	$\mathrm{mmHg\ s\ mL^{-1}}$	$E_{\mathrm{LA}}^{\mathrm{act,max}}$	0.07	$\mathrm{mmHg\ mL^{-1}}$
$C_{\mathrm{AR}}^{\mathrm{SYS}}$	1.2	$\mathrm{mL\ mmHg^{-1}}$	$E_{\mathrm{RA}}^{\mathrm{act,max}}$	0.06	$\mathrm{mmHg\ mL^{-1}}$
$C_{\mathrm{AR}}^{\mathrm{PUL}}$	10.0	$\mathrm{mL\ mmHg^{-1}}$	$E_{\mathrm{RV}}^{\mathrm{act,max}}$	0.55	$\mathrm{mmHg\ mL^{-1}}$
$C_{\mathrm{VEN}}^{\mathrm{SYS}}$	60.0	$\mathrm{mL\ mmHg^{-1}}$	$V_{0,\mathrm{LA}}$	4.0	mL
$C_{\mathrm{VEN}}^{\mathrm{PUL}}$	16.0	$\mathrm{mL\ mmHg^{-1}}$	$V_{0,\mathrm{RA}}$	4.0	mL
$L_{\mathrm{AR}}^{\mathrm{SYS}}$	$5 \cdot 10^{-3}$	$\mathrm{mmHg\ s^2\ mL^{-1}}$	$V_{0,\mathrm{RV}}$	16.0	mL
$L_{\mathrm{AR}}^{\mathrm{PUL}}$	$5 \cdot 10^{-4}$	$\mathrm{mmHg\ s^2\ mL^{-1}}$	**Cardiac valves**		
$L_{\mathrm{VEN}}^{\mathrm{SYS}}$	$5 \cdot 10^{-4}$	$\mathrm{mmHg\ s^2\ mL^{-1}}$	R_{min}	0.007 5	$\mathrm{mmHg\ s\ mL^{-1}}$
$L_{\mathrm{VEN}}^{\mathrm{PUL}}$	$5 \cdot 10^{-4}$	$\mathrm{mmHg\ s^2\ mL^{-1}}$	R_{max}	75 006.2	$\mathrm{mmHg\ s\ mL^{-1}}$

References

[1] H. Arevalo, F. Vadakkumpadan, E. Guallar, et al., Arrhythmia risk stratification of patients after myocardial infarction using personalized heart models, Nat. Commun. 7 (2016) 113–128.

[2] D. Arndt, W. Bangerth, B. Blais, et al., The deal.II library, version 9.2, J. Numer. Math. 28 (3) (2020) 131–146.

[3] T. Arts, T. Delhaas, P. Bovendeerd, et al., Adaptation to mechanical load determines shape and properties of heart and circulation: the circadapt model, Am. J. Physiol. Heart Circ. Physiol. 288 (2005) H1943–H1954.

[4] C.M. Augustin, M.A.F. Gsell, E. Karabelas, et al., A computationally efficient physiologically comprehensive 3D–0D closed-loop model of the heart and circulation, Comput. Methods Appl. Mech. Eng. 386 (2021) 114092.

[5] C. Bartolucci, E. Passini, J. Hyttinen, et al., Simulation of the effects of extracellular calcium changes leads to a novel computational model of human ventricular action potential with a revised calcium handling, Front. Physiol. 11 (2020) 314.

[6] M.B. Bastos, D. Burkhoff, J. Maly, et al., Invasive left ventricle pressure–volume analysis: overview and practical clinical implications, Eur. Heart J. 41 (12) (2019) 1286–1297.

[7] J.D. Bayer, R.C. Blake, G. Plank, N. Trayanova, A novel rule-based algorithm for assigning myocardial fiber orientation to computational heart models, Ann. Biomed. Eng. 40 (10) (2012) 2243–2254.

[8] P.J. Blanco, R.A. Feijóo, A 3D-1D-0D computational model for the entire cardiovascular system, in: E. Dvorking, M. Goldschmit, M. Storti (Eds.), Computational Mechanics, vol. 29, 2010, pp. 5887–5911.

[9] A. Bueno-Orovio, E.M. Cherry, F.H. Fenton, Minimal model for human ventricular action potentials in tissue, J. Theor. Biol. 253 (2008) 544–560.

[10] N. Cedilnik, J. Duchateau, R. Dubois, et al., Fast personalized electrophysiological models from computed tomography images for ventricular tachycardia ablation planning, EP Europace 20 (suppl 3) (2018) iii94–iii101.

[11] D. Chapelle, M.A. Fernández, J.F. Gerbeau, et al., Numerical simulation of the electromechanical activity of the heart, Int. Conf. Funct. Imag.Model.Heart 5528 (2009) 357–365.

[12] P. Colli Franzone, L.F. Pavarino, S. Scacchi, Mathematical Cardiac Electrophysiology, vol. 13, Springer, 2014.

[13] P. Colli Franzone, L.F. Pavarino, S. Scacchi, Effects of mechanical feedback on the stability of cardiac scroll waves: a bidomain electro-mechanical simulation study, Chaos 27 (2017), 093905.

[14] P. Colli Franzone, L.F. Pavarino, S. Scacchi, A numerical study of scalable cardiac electro-mechanical solvers on HPC architectures, Front. Physiol. 9 (2018) 268.

[15] A. Collin, S. Imperiale, P. Moireau, et al., Apprehending the effects of mechanical deformations in cardiac electrophysiology: a homogenization approach, Math. Model Methods Appl. Sci. 29 (13) (2019) 2377–2417.

[16] R. Coppini, C. Ferrantini, L. Yao, et al., Late sodium current inhibition reverses electromechanical dysfunction in human hypertrophic cardiomyopathy, Circulation 127 (5) (2013) 575–584.

[17] F.S. Costabal, F.A. Concha, D.E. Hurtado, et al., The importance of mechano-electrical feedback and inertia in cardiac electromechanics, Comput. Methods Appl. Mech. Eng. 320 (2017) 352–368.

[18] F.S. Costabal, D.E. Hurtado, E. Kuhl, Generating purkinje networks in the human heart, J. Biomech. 49 (2016) 2455–2465.

[19] D. Deng, A. Prakosa, J. Shade, et al., Sensitivity of ablation targets prediction to electrophysiological parameter variability in image-based computational models of ventricular tachycardia in post-infarction patients, Front. Physiol. 10 (2019) 628.

[20] S. Doll, K. Schweizerhof, On the development of volumetric strain energy functions, J. Appl. Mech. 67 (2000) 17–21.

[21] A.E. Epstein, et al., Acc/aha/hrs 2008 guidelines for device-based therapy of cardiac rhythm abnormalities: a report of the american college of cardiology/american heart association task force on practice guidelines (writing committee to revise the acc/aha/naspe 2002 guideline update for implantation of cardiac pacemakers and antiarrhythmia devices): developed in collaboration with the american association for thoracic surgery and society of thoracic surgeons, Circulation 117 (2008) e350–e408.

[22] A. Frontera, S. Pagani, L.R. Limite, et al., Outer loop and isthmus in ventricular tachycardia circuits: characteristics and implications, Heart Rhythm 17 (10) (2020) 1719–1728.

[23] A. Gerbi, L. Dedè, A. Quarteroni, A monolithic algorithm for the simulation of cardiac electromechanics in the human left ventricle, Mathematics in Engineering 1 (2018) 1–37.

[24] J.M. Guccione, A.D. McCulloch, Finite element modeling of ventricular mechanics, in: Theory of Heart, Springer, 1991, pp. 121–144.

[25] J.M. Guccione, A.D. McCulloch, L.K. Waldman, Passive material properties of intact ventricular myocardium determined from a cylindrical model, J. Biomech. Eng. 113 (1991) 42–55.

[26] A. Hazim, Y. Belhamadia, S. Dubljevic, A simulation study of the role of mechanical stretch in arrhythmogenesis during cardiac alternans, Biophys. J. 120 (1) (2021) 109–121.

[27] M. Hirschvogel, M. Bassilious, L. Jagschies, et al., A monolithic 3D-0D coupled closed-loop model of the heart and the vascular system: experiment-based parameter estimation for patient-specific cardiac mechanics, Int. J. Numer. Methods.Biomed. Eng. 33 (2017), e2842.

[28] G.A. Holzapfel, R.W. Ogden, Constitutive modelling of passive myocardium: a structurally based framework for material characterization, Phil. Trans. Math. Phys. Eng. Sci. 367 (2009) 3445–3475.

[29] Zygote Media Group Inc, Zygote Solid 3D Heart Generation II Development Report, Technical Report, 2014.

[30] X. Jie, V. Gurev, N. Trayanova, Mechanisms of mechanically induced spontaneous arrhythmias in acute regional ischemia, Circ. Res. 106 (1) (2010) 185–192.

[31] J.P. Keener, J. Sneyd, Mathematical Physiology, ume 1, Springer, 2009.

[32] R.H. Keldermann, M.P. Nash, H. Gelderblom, et al., Electromechanical wavebreak in a model of the human left ventricle, Am. J. Physiol. Heart Circ. Physiol. 299 (1) (2010) H134–H143.

[33] R.C.P. Kerckhoffs, M.L. Neal, Q. Gu, et al., Coupling of a 3d finite element model of cardiac ventricular mechanics to lumped systems models of the systemic and pulmonic circulation, Ann. Biomed. Eng. 35 (1–18) (2007).

[34] P. Kohl, F. Sachs, M.R. Franz, Cardiac Mechano-Electric Coupling and Arrhythmias, Oxford University Press, 2013.

[35] S. Land, S. Park-Holohan, N.P. Smith, et al., A model of cardiac contraction based on novel measurements of tension development in human cardiomyocytes, J. Mol. Cell. Cardiol. 106 (2017) 68–83.

[36] M. Landajuela, C. Vergara, A. Gerbi, et al., Numerical approximation of the electromechanical coupling in the left ventricle with inclusion of the purkinje network, Int. J. Numer. Methods.Biomed. Eng. 34 (2018), e2984.

[37] F. Levrero-Florencio, F. Margara, E. Zacur, et al., Sensitivity analysis of a strongly-coupled human-based electromechanical cardiac model: effect of mechanical parameters on physiologically relevant biomarkers, Comput. Methods Appl. Mech. Eng. 361 (2020) 112762.

[38] C. Luo, Y. Rudy, A dynamic model of the cardiac ventricular action potential. I. simulations of ionic currents and concentration changes, Circ. Res. 74 (1994) 1071–1096.

[39] S.A. Niederer, P.J. Hunter, N.P. Smith, A quantitative analysis of cardiac myocyte relaxation: a simulation study, Biophys. J. 90 (5) (2006) 1697–1722.

[40] S.A. Niederer, G. Plank, P. Chinchapatnam, et al., Length-dependent tension in the failing heart and the efficacy of cardiac resynchronization therapy, Cardiovasc. Res. 89 (2011) 336–343.

[41] F. Nobile, A. Quarteroni, R. Ruiz-Baier, An active strain electromechanical model for cardiac tissue, Int. J. Numer. Methods.Biomed. Eng. 28 (2012) 52–71.

[42] R.W. Ogden, Non-linear Elastic Deformations, Courier Corporation, 1997.

[43] S.H. Peng, W.V. Chang, A compressible approach in finite element analysis of rubber-elastic materials, Comput. Struct. 62 (1997) 573–593.

[44] M.R. Pfaller, J.M. Hörmann, M. Weigl, et al., The importance of the pericardium for cardiac biomechanics: from physiology to computational modeling, Biomech. Model. Mechanobiol. 18 (2019) 503–529.

[45] R. Piersanti, P.C. Africa, M. Fedele, et al., Modeling cardiac muscle fibers in ventricular and atrial electrophysiology simulations, Comput. Methods Appl. Mech. Eng. 373 (2021) 113468.

[46] R. Piersanti, F. Regazzoni, M. Salvador, et al., 3D-0D Closed-Loop Model for the Simulation of Cardiac Electromechanics, MOX Report 57, Politecnico di Milano, 2021.

[47] A. Prakosa, H. Arevalo, D. Dongdong, et al., Personalized virtual-heart technology for guiding the ablation of infarct-related ventricular tachycardia, Nature Biomedical Engineering 2 (2018) 732–740.

[48] A. Quarteroni, Numerical Models for Differential Problems, vol. 2, Springer, 2009.

[49] A. Quarteroni, L. Dedè, A. Manzoni, C. Vergara, *Mathematical modelling of the Human Cardiovascular System: Data, Numerical Approximation, Clinical Applications*. Cambridge Monographs on Applied and Computational Mathematics, Cambridge University Press, 2019.

[50] A. Quarteroni, T. Lassila, S. Rossi, R. Ruiz-Baier, Integrated Heart—coupling multiscale and multiphysics models for the simulation of the cardiac function, Comput. Methods Appl. Mech. Eng. 314 (2017) 345–407.

[51] A. Quarteroni, A. Veneziani, C. Vergara, Geometric multiscale modeling of the cardiovascular system, between theory and practice, Comput. Methods Appl. Mech. Eng. 302 (2016) 193–252.

[52] F. Regazzoni, L. Dedè, A. Quarteroni, Biophysically detailed mathematical models of multiscale cardiac active mechanics, PLoS Comput. Biol. 16 (2020), e1008294.

[53] F. Regazzoni, L. Dedè, A. Quarteroni, Machine learning of multiscale active force generation models for the efficient simulation of cardiac electromechanics, Comput. Methods Appl. Mech. Eng. 370 (2020) 113268.

[54] F. Regazzoni, A. Quarteroni, Accelerating the convergence to a limit cycle in 3d cardiac electromechanical simulations through a data-driven 0d emulator, Comput. Biol. Med. 135 (2021) 104641.

[55] F. Regazzoni, A. Quarteroni, An oscillation-free fully staggered algorithm for velocity-dependent active models of cardiac mechanics, Comput. Methods Appl. Mech. Eng. 373 (2021) 113506.

[56] F. Regazzoni, M. Salvador, P.C. Africa, et al., A Cardiac Electromechanics Model Coupled with a Lumped Parameters Model for Closed-Loop Blood Circulation. Part I: Model Derivation, MOX Report 79, Politecnico di Milano, 2020.

[57] F. Regazzoni, M. Salvador, P.C. Africa, et al., A Cardiac Electromechanics Model Coupled with a Lumped Parameters Model for Closed-Loop Blood Circulation. Part II: Numerical Approximation. MOX Report 78, Politecnico di Milano, 2020.

[58] J.J. Rice, F. Wang, D.M. Bers, P.P. de Tombe, Approximate model of cooperative activation and crossbridge cycling in cardiac muscle using ordinary differential equations, Biophys. J. 95 (5) (2008) 2368–2390.

[59] S. Rossi, T. Lassila, R. Ruiz-Baier, et al., Thermodynamically consistent orthotropic activation model capturing ventricular systolic wall thickening in cardiac electromechanics, Eur. J. Mech. Solid. 48 (2014) 129–142.

[60] R. Ruiz-Baier, A. Gizzi, S. Rossi, et al., Mathematical modelling of active contraction in isolated cardiomyocytes, Math. Med. Biol.: a Journal of the IMA 31 (2014) 259–283.

[61] M. Salvador, L. Dedè, A. Quarteroni, An intergrid transfer operator using radial basis functions with application to cardiac electromechanics, Comput. Mech. 66 (2020) 491–511.

[62] M. Salvador, M. Fedele, P.C. Africa, et al., Electromechanical modeling of human ventricles with ischemic cardiomyopathy: numerical simulations in sinus rhythm and under arrhythmia, Comput. Biol. Med. 136 (2021) 104674.
[63] F.H. Samie, J. Jalife, Mechanisms underlying ventricular tachycardia and its transition to ventricular fibrillation in the structurally normal heart, Cardiovasc. Res. 50 (2001) 242–250.
[64] M. Strocchi, M.A.F. Gsell, C.M. Augustin, et al., Simulating ventricular systolic motion in a four-chamber heart model with spatially varying robin boundary conditions to model the effect of the pericardium, J. Biomech. 101 (2020) 109645.
[65] P. Taggart, P.M. Sutton, Cardiac mechano-electric feedback in man: clinical relevance, Prog. Biophys. Mol. Biol. 71 (1) (1999) 139–154.
[66] K.H.W.J. ten Tusscher, A.V. Panfilov, Alternans and spiral breakup in a human ventricular tissue model, Am. J. Physiol. Heart Circ. Physiol. 291 (2006) H1088–H1100.
[67] V. Timmermann, L.A. Dejgaard, K. Haugaa, et al., An integrative appraisal of mechano-electric feedback mechanisms in the heart, Prog. Biophys. Mol. Biol. 130 (Pt B) (2017) 404–417.
[68] J. Tomek, A. Bueno-Orovio, E. Passini, et al., Development, calibration, and validation of a novel human ventricular myocyte model in health, disease, and drug block, Elife 8 (2019), e48890.
[69] N. Trayanova, Whole-heart modeling: applications to cardiac electrophysiology and electromechanics, Circ. Res. 108 (2011) 113–128.
[70] N. Trayanova, W. Li, J. Eason, P. Kohl, Effect of stretch-activated channels on defibrillation efficacy, Heart Rhythm 1 (67–77) (2004), 06.
[71] M. Varela, A. Roy, J. Lee, A survey of pathways for mechano-electric coupling in the atria, Prog. Biophys. Mol. Biol. 159 (2021) 136–145.
[72] C. Vergara, S. Palamara, D. Catanzariti, et al., Patient-specific generation of the purkinje network driven by clinical measurements of a normal propagation, Med. Biol. Eng. Comput. 52 (2014) 813–826.